SANDIA REPORT

SAND2014-17252
Unlimited Release
Printed September 2014

Structural Health Monitoring for Impact Damage in Composite Structures

Raymond M. Bond, Douglas E. Adams, Dennis P. Roach

Prepared by
Sandia National Laboratories
Albuquerque, New Mexico 87185 and Livermore, California 94550

Sandia National Laboratories is a multi-program laboratory managed and operated by Sandia Corporation, a wholly owned subsidiary of Lockheed Martin Corporation, for the U.S. Department of Energy's National Nuclear Security Administration under contract DE-AC04-94AL85000.

Issued by Sandia National Laboratories, operated for the United States Department of Energy by Sandia Corporation.

Available to DOE and DOE contractors from
U.S. Department of Energy
Office of Scientific and Technical Information
P.O. Box 62
Oak Ridge, TN 37831

Telephone: (865) 576-8401
Facsimile: (865) 576-5728
E-Mail: reports@adonis.osti.gov
Online ordering: http://www.osti.gov/bridge

Available to the public from
U.S. Department of Commerce
National Technical Information Service
5285 Port Royal Rd
Springfield, VA 22161

Telephone: (800) 553-6847
Facsimile: (703) 605-6900
E-Mail: orders@ntis.fedworld.gov
Online ordering: http://www.ntis.gov/help/ordermethods.asp?loc=7-4-0#online

SAND2014-17252
Unlimited Release
Printed September 2014

Structural Health Monitoring for Impact Damage in Composite Structures

Ray M. Bond, Douglas E. Adams
School of Mechanical Engineering
Purdue University
585 Purdue Mall
West Lafayette, IN, 47907-2088
rmbond@purdue.edu
deadams@purdue.edu

Dennis P. Roach
Transportation Safeguards & Surety
Sandia National Laboratories
P.O. Box 5800
Albuquerque, NM, 87185
dproach@sandia.gov

Abstract

Composite structures are increasing in prevalence throughout the aerospace, wind, defense, and transportation industries, but the many advantages of these materials come with unique challenges, particularly in inspecting and repairing these structures. Because composites often undergo sub-surface damage mechanisms which compromise the structure without a clear visual indication, inspection of these components is critical to safely deploying composite replacements to traditionally metallic structures. Impact damage to composites presents one of the most significant challenges because the area which is vulnerable to impact damage is generally large and sometimes very difficult to access. This work seeks to further evolve identification technology by developing a system which can detect the impact load location and magnitude in real time, while giving an assessment of the confidence in that estimate. Furthermore, we identify ways by which impact damage could be more effectively identified by leveraging impact load identification information to better characterize damage. The impact load identification algorithm was applied to a commercial scale wind turbine blade, and results show the capability to detect impact magnitude and location using a single accelerometer, regardless of sensor location. A technique for better evaluating the uncertainty of the impact estimates was developed by quantifying how well the impact force estimate meets the assumptions underlying the force estimation technique. This uncertainty quantification technique was found to reduce the 95% confidence interval by more than a factor of two for impact force estimates showing the least uncertainty, and widening the 95% confidence interval by a factor of two for the most uncertain force estimates, avoiding the possibility of understating the uncertainty associated with these estimates. Linear vibration based damage detection techniques were investigated in the context of structural stiffness reductions and impact damage.

A method by which the sensitivity to damage could be increased for simple structures was presented, and the challenges of applying that technique to a more complex structure were identified. The structural dynamic changes in a weak adhesive bond were investigated, and the results showed promise for identifying weak bonds that show little or no static reduction in stiffness. To address these challenges in identifying highly localized impact damage, the possibility of detecting damage through nonlinear dynamic characteristics was also identified, with a proposed technique which would leverage impact location estimates to enable the detection of impact damage. This nonlinear damage identification concept was evaluated on a composite panel with a substructure disbond, and the results showed that the nonlinear dynamics at the damage site could be observed without a baseline healthy reference. By further developing impact load identification technology and combining load and damage estimation techniques into an integrated solution, the challenges associated with impact detection in composite structures can be effectively solved, thereby reducing costs, improving safety, and enhancing the operational readiness and availability of high value assets.

Acknowledgment

This work was sponsored by Sandia National Laboratories under a Laboratory Directed Research and Development (LDRD) program as part of the Sandia Campus Executive program. The Sandia National Laboratories campus executive for Purdue University is Dr. Paul Hommert, and the deputy campus executive is Dr. Marcey Hoover. Their generous support is gratefully acknowledged.

This page intentionally left blank.

Contents

Figures

Tables

Nomenclature

ADC Analog to Digital Converter

ARMA Auto-Regressive Moving Average

CBM Condition-Based Maintenance

DAQ Data Acquisition

DFT Discrete Fourier Transform

DOF Degree of Freedom

FFT Fast Fourier Transform

FRF Frequency Response Function

FIR Finite Impulse Response

IDFT Inverse Discrete Fourier Transform

IFFT Inverse Fast Fourier Transform

IIR Infinite Impulse Response

IRF Impulse Response Function

MIMO Multiple Inputs, Multiple Outputs

NDE Non-Destructive Evaluation

NIFO Non-linear Identification through Feedback of the Outputs

SHM Structural Health Monitoring

SVD Singular Value Decomposition

1 Introduction

Composite materials are becoming more prevalent, particularly in high performance weight-critical applications, because their specific strength and stiffness can exceed that of metals and engineers can tailor composite material properties to specific applications in ways that would not be possible with isotropic materials. However, the numerous advantages of composite materials are not without their downsides. One of the most important challenges to deploying composite aircraft is monitoring the health of composite structure and identifying complex damage mechanisms which are often without any clear visual indication. Impact damage is especially of concern because composite laminates are susceptible to sub-surface impact damage, such as delamination, substructure disbonds, or, in the case of sandwich composites, core-crushing.

1.1 Motivation for impact damage monitoring

Damaging impacts can occur throughout the lifecycle of the structure, and identifying the location and severity of these impacts is critical to assessing structural health. When the composite structure is accessible for inspection, an impact monitoring system has the potential to increase operational readiness by identifying specific areas where damage is likely, and therefore limit the need for wide-area inspections. When the structure is not accessible for inspection, an impact monitoring system can be even more useful by providing information which can be used to estimate the damage state and predict the remaining useful life of that component.

Impact Damage Monitoring for Aircraft

The lifecycle costs of aviation assets can exceed 98% of the total cost of the maintenance and purchase prices of the asset. Military aircraft experience particularly high lifecycle costs, but as commercial aircraft begin to adapt some of the composite technology used in military aircraft, the associated costs of these aircraft are likely to increase if inspection and structural health monitoring technology fails to adapt to the new challenges of these technologies. One important way that structural health monitoring technology could reduce operational costs of these aircraft is by identifying impact loads on composite structures, and determining where impact damage may have occurred.

Impact damage is one of the most prevalent sources of damage in composite aircraft, so the knowledge of where potentially damaging impacts have occurred could significantly reduce the

need for time-consuming wide-area inspections and the associated cost. For example, one study estimated that a fully autonomous impact sensing system on a composite fighter jet could reduce inspection time by as much as 50% [5]. A large scale Sandia lead SHM survey of aviation industry stakeholders, including operators, manufacturers, regulators, and maintainers indicated that 64.4% of those surveyed were interested in identifying impact events using SHM technology [46]. In addition, the same study showed that more than 83% of respondents wanted to detect disbonds and delaminations in aviation assets, which are sub-surface damage mechanisms that can originate from impacts.

Impact Damage Monitoring for Wind Turbine Blades

On any structure, inspection for impact damage in composites is often very time consuming and requires multiple inspection techniques to accurately identify the location and extent of these numerous damage mechanisms [29]. Inspection of large wind turbine rotor blades, however, is particularly expensive and challenging, due to the size and inaccessibility of these blades. The inspection burden could be significantly alleviated by identifying the location and magnitude of applied impact loads, which makes wind turbine blades ideal applications for composite structural health monitoring techniques.

Damaging impact loads are a concern for wind turbine blades both while in operation and during transport [18, 58]. Some examples of impact loads in operation are hail, bird strikes, airborne objects, or ice shedding from other blades. One study found that 7% of unforeseen malfunctions in 1.5MW wind turbines operating in Germany were attributed to rotor blade problems, with an average down time of four days per failure[27]. Unforeseen repairs on wind turbines are especially costly, as these repairs are around 500% more expensive than regularly scheduled maintenance[2]. An impact load estimation technique such as the one presented here has the potential to provide maintainers with the information they need to limit the progression of damage by way of prompt repairs, schedule maintenance in advance, and track the loading history of blades to identify problematic trends.

1.2 Review of Existing Impact Identification Technology

Although impact force estimation has been widely studied, significant limitations remain, and other techniques have not been shown to effectively estimate the location and magnitude of impact loads to large structures of arbitrary geometry using very few sensors. Impact identification approaches

differ in a number of aspects, including the type of sensor technology used, the algorithm used for identifying the location of impact, and the underlying model used for inverse force estimation.

Impact Identification Algorithms

Impact identification algorithms are generally classified into two broad categories: 1) those based on physical models of the structure, and 2) those based on black box computational methods, most notably artificial neural networks. Artificial neural networks have been widely utilized in this area because many model-based techniques can only effectively locate impacts to simple structures where a tractable mathematical solution exists (e.g. beams or plates) [43, 11, 62, 26, 21]. Because artificial neural network based techniques do not rely on a physical model of the system, this class of techniques can locate impacts to complex geometry through the use of adequate training data, sensor density, and careful selection of initial conditions [51, 26]. Although neural network based approaches can be effective on arbitrary structures, as Sharif-Khodaei notes in his article relating to artificial neural network based impact identification, a vast library of training data from impacts of representative mass and velocities of interest would be required to effectively locate all impacts of interest[51]. Considering that the impacts of interest are potentially damaging, collecting this library of training data non destructively would not be possible. While finite-element simulations can be used to train artificial neural networks with a wide variety of impacts, the applicability of finite element based neural networks to physical systems has yet to be firmly established.

Model-based impact identification algorithms do not have the same drawbacks as neural network based techniques, and a number of modern techniques have been developed which apply to complex structures, such as stiffened composite panels, helicopter rotor blades, or filament-wound canisters. These model based techniques appear to be more promising than artificial neural network based techniques because they do not rely on training data from impacts with damaging energy levels, provided that linearity of the system remains an adequate assumption for impacts of interest.

Among model-based impact identification techniques, methods vary in the underlying model used for inversion, the sensor technology employed, the inversion technique used, and the algorithm for localizing impacts. The most fundamental differences between techniques are the underlying physical model and the algorithm for localizing impacts.

The choice of model affects both the difficulty of adapting the technique to different structures and the spatial resolution of impact location estimates. Some techniques, for instance the technique presented by Seydel and Chang [48, 49], express the system dynamics as continuous functions of

the impact location coordinates. By using iterative location identification procedures with continuous models, arbitrarily fine spatial resolution is theoretically possible. The downside to these iterative techniques is that a reasonably accurate initial location estimate is needed to converge to the correct impact location. To estimate the initial position, techniques based on wave arrival time [48, 49] or sensor response amplitude at a grid of sensors [45, 44] can be used. While these approaches to estimate initial position for iteration are effective, they usually necessitate a spatially dense grid of sensors. The requirement of an initial position estimate for these iterative techniques is one of the main reasons that these techniques generally require a spatially dense grid of sensors.

An alternative to the iterative approach is to discretize the possible impact locations into a finite set of possible impact locations, usually on an evenly spaced grid. While this discretization limits the fidelity of the location estimate, the impact location can be estimated without iteration, thereby eliminating the need for a reasonably accurate initial guess of the impact location. Without the need for an initial condition for iteration, no grid of sensors is inherently required when this approach is used. This single stage solution procedure has been shown to be effective in locating impacts with few sensors. Stites, Yoder and Adams have shown this approach to be effective at locating impacts to a filament wound rocket motor casing with a single sensor [54, 41, 53, 65], and the same group also applied this type of technique to a helicopter main rotor blade with a single sensor [13]. Hu and Fukunaga have presented a similar approach of discretizing the system and finding the best fit point, using four piezoelectric sensors and models based on finite element modeling [31, 30, 22] and related works have shown the same technique to be effective using experimentally determined models [4, 8]. Because the present work uses a single sensor for impact identification, we use the approach of localizing the impact to the nearest predefined grid point. Although other studies have shown the ability to improve the accuracy of spatially discretized impact identification techniques through interpolating frequency response function estimates [65, 13], this study will simply focus on identifying impacts to the nearest trained grid location without any additional interpolation.

1.3 Uncertainty Quantification for Impact Identification

The first portion of this impact damage estimation is determining the location and magnitude of any impact loading events that may have caused damage. The entropy-based impact identification strategy that we have presented has been shown to effectively locate and quantify impact loads, but little had been done to formally quantify the uncertainty in the force estimates. This study will consider the effects of a number of potential factors such as accelerometer location, type of sensor technology, number of channels of response data, and orientation of these sensors. Understanding the uncertainty is critical to making meaningful decisions based on these estimates, so this work

evaluates the magnitude of the uncertainty and also assesses a method to better determine the uncertainty of a particular force estimate in real time.

One approach to quantifying the impact load uncertainty is to simply evaluate the error across a large set of validation tests. Prior to the study described here, this approach has been the only one that we have used to quantify the range of force estimation errors that can be expected. The new approach that we develop here classifies the set of validation tests into ranges based on the entropy of the impact force estimate. Because the impact identification algorithm assumes an impulsive force, and the entropy of the force estimate is a way of evaluating the impulsivity of that estimate, the measure of entropy is essentially a measure of how well the estimate fits the assumptions of the algorithm. Therefore, the expected trend is that the better the estimate fits the assumptions, the less uncertainty in that estimate. We will show how in a simple analytical example, the entropy of impact force estimates increases with experimental error, and then we will validate this approach by applying this impact identification technology to a retired commercial wind turbine blade.

1.4 Integrated Impact Load and Damage Identification Concept

Health monitoring of a structure can be broken down into two primary objectives: 1) identifying the loading history of the structure, and 2) identifying (including tracking) the damage state of the structure. In general, these two objectives are achieved with distinct load identification methods and damage detection and/or inspection techniques. Combining these two capabilities by first identifying impact loads and locations, and then leveraging that information to determine whether the structure has sustained damage, holds the potential to increase the accuracy and expand the applicability of damage detection techniques.

Most current SHM technology proposed for detecting damage or flaws in composite structures require dense arrays of transducers to achieve the desired level of accuracy. The cost, weight, and complexity of implementing a dense grid of transducers present significant barriers to implementing systems of this type on a large scale for today's large composite structures. The requisite sensor density therefore practically limits many of these approaches to "hot spot" detection, that is, small scale monitoring of areas where damage is likely to occur, or to safety critical areas which are difficult to otherwise monitor. While there is certainly substantial value in monitoring critical areas of the structure, these types of approaches are poorly suited to impact damage detection, because impacts can occur over a very wide area of the structure. In essence, most current SHM products that detect damage are essentially nondestructive inspection (NDI) technologies installed on the structure. This approach enables monitoring areas which could not otherwise be easily inspected

and allows for timely information on the structural health, potentially increasing operational readiness and reducing costs associated with downtime. However, these products neither acknowledge operating loads that affect the health of a structure nor take advantage of their effectiveness in aiding damage detection techniques. Although some SHM systems attempt to use fewer transducers to detect damage in large areas, these technologies do not directly take into account the effects of operational loading on in-situ damage detection algorithms.

This work will evaluate how utilizing impact location information, estimated through our impact identification technique, can improve the ability to detect impact damage. To that end, this report considers two classes of damage detection technologies: those based on linear vibration characteristics, and those based on nonlinear vibration characteristics, with a focus on how knowledge of the location and nature of potential damage might improve the accuracy and expand the capability of these systems.

2 Impact Identification Theory

2.1 Overview

The theory used to identify the location and magnitude of impact loads acting on a structure is detailed in this chapter. The process involves several steps that are conducted prior to monitoring for impacts as well as steps that are conducted to acquire and process data once an impact is detected. The process is illustrated in Figure 1. First, modal impact testing is used to characterize the forced response of the discretized underlying model of the structure. Several sets of impact force and acceleration response data are averaged for each possible impact point to estimate the frequency response function between that impact location and the response measurement locations/directions. After estimating the frequency response functions, a set of assumptions along with the FRF model, which is constructed from the training data, are used to solve an overdetermined inverse problem. The pseudoinverse, used to solve the systems of equations of interest, is calculated in advance of monitoring for impacts, and the results are saved into memory. When an impact is detected, the impact response measurements are pre-processed and the response spectra due to a single impact are passed to the force spectrum estimation algorithm. By combining the measured responses and the pseudoinverse formed using the FRF model based on the training data, the impact force is estimated assuming that it acted at each of the possible input measurement degrees of freedom. Once these force estimates are calculated, the algorithm then determines which force estimate most likely corresponds to the actual impact location. The estimated force for the selected location is then further post-processed to refine the force estimate, and the process is completed.

2.2 Indirect Force Estimation Theory

Discretized Frequency Response Function Model

In order to explain the technical details of the indirect force identification methods that are used, a discussion of the implicit underlying forced response model is given here with an emphasis on the limitations associated with representing a continuous structure by a discretized model. A simple example of a cantilevered beam will be used for illustration, as depicted in Figure 2. This beam is a continuous structure which can be excited by a forcing function that varies with both time and position along the beam. The response of the structure changes with position along the beam.

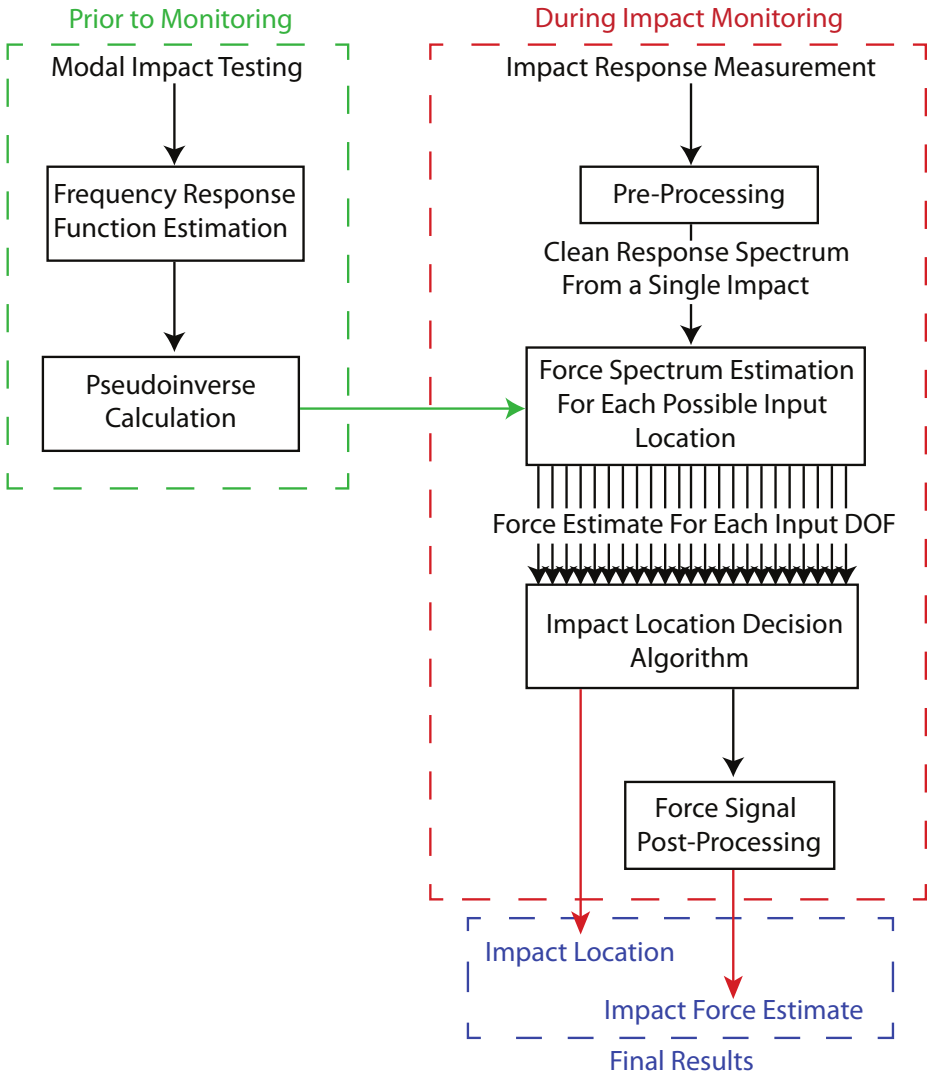

Figure 1: The Impact Identification Process Is Illustrated Here, Showing The Necessary Steps Before And During Impact Monitoring.

Because there are infinitely many degrees of freedom, there are infinitely many modes of vibration.

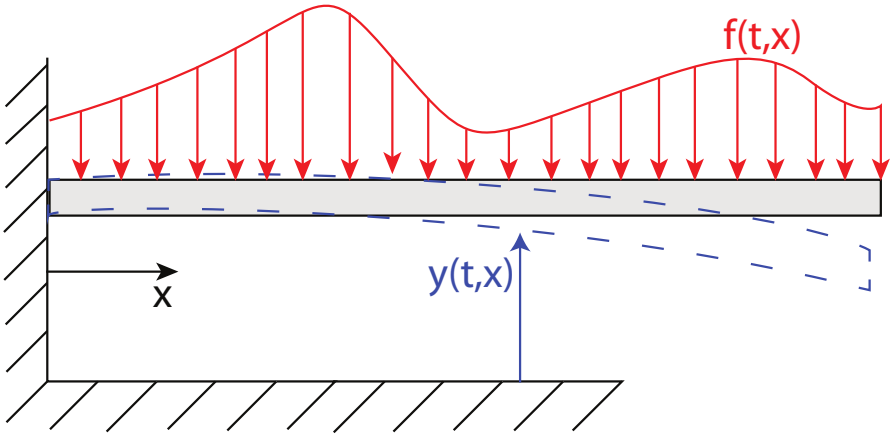

Figure 2: A Cantilevered Beam, As Illustrated Here, Is Used To Explain The Discretization Process Of A Continuous Structure.

The model used in this work is a data-driven model determined solely from measurements, rather than a first-principles model of the physics of the structure; therefore, the forced response at infinitely many degrees of freedom cannot be captured using this empirical model. The data-driven model of the structure is in a form where the response (or forcing function) can be estimated based on measurements alone. The continuous representation of the structure must be discretized both temporally and spatially in order to create this data-driven model, as illustrated in Figure 3. Spatially, the model must be reduced to a finite number of measurement degrees of freedom. In the case of the present example, six degrees of freedom are used, and at each location, a force acts and the system responds at each point in time. The time histories are discretized temporally by replacing the continuous time variable t with t_n, where $t_n = n\Delta_t$, $n = 0, 1, \ldots, N$ and $\Delta_t = 1/f_s$, where f_s is the sampling frequency.

This discrete form of the model must now also be limited in terms of the number of measurements available. The measurement degrees of freedom are defined by the number of output sensor channels that are available and the number of grid points that are impacted when modal impact testing is conducted to gather the training data. The number of output measurement degrees of freedom are represented by N_o, and the number of input measurement degrees of freedom are called N_i. When monitoring for impacts, the selection of a large N_i does not add any hardware cost; rather, it requires more points on the structure to be impacted during modal impact testing in order to generate the training data. The addition of output degrees of freedom, N_o, however, requires that additional sensors be placed on the structure leading to additional data acquisition equipment. Therefore, N_o will be much less than N_i in this case. The example beam structure in the final configuration that is representative of an impact identification configuration is shown

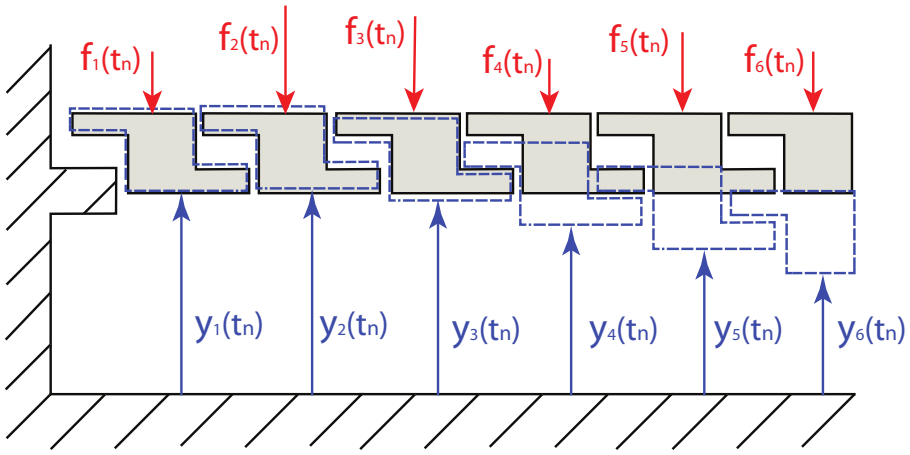

Figure 3: This Discrete Representation Of The Example Cantilevered Beam Is In A Form That Can Be Characterized By Measurements Alone.

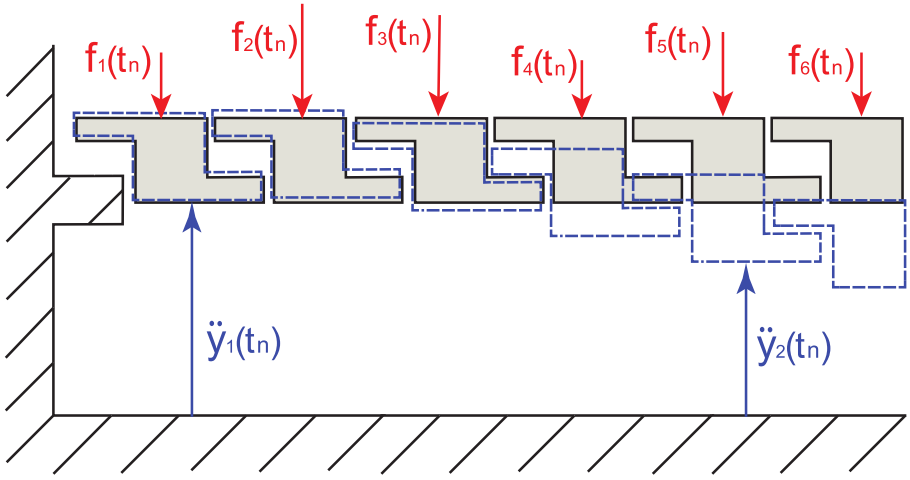

Figure 4: The Example Beam Structure Is Shown In A Configuration Representative Of An Impact Identification Setup.

in Figure 4. The key differences between the discretized model that will be used in the impact identification technique and the original discretized model is that (a) the beam structure is limited to $N_o = 2$ output measurement degrees of freedom, and (b) the acceleration response is measured in the beam, as it will be in the actual test setup using accelerometers, rather than the displacement response. Although the output measurement degrees of freedom are a subset of the input degrees of freedom in this case, that is not generally the case when tri-axial accelerometers are used to record the response. When tri-axial accelerometers are used, the forced degrees of freedom are limited to the normal direction whereas some response degrees of freedom will be measured in directions perpendicular to the normal direction.

Sparse Sensing Impact Force Estimation Theory

The impact identification algorithm that is developed here indirectly estimates a localized applied force by inverting a data training model that is constructed empirically. In order to apply this method, a set of assumptions must be applied to formulate an overdetermined inverse problem that is suitable for inversion with a pseudoinverse to solve for the best-fit estimate of the forcing function. With no assumptions or constraints applied, the inverse problem is underdetermined with an infinite number of solutions. This example presents the approach assuming N_o acceleration response measurements are available.

The frequency band is limited to $\{0, f_{max}\}$ and the number of frequency points is reduced to N_f, yielding a frequency resolution of Δ_f. N_i discrete points are defined where a force can be applied. This underdetermined system can be reduced to N_f systems of equations as follows:

$$\begin{Bmatrix} A_1(n\Delta_f) \\ A_2(n\Delta_f) \\ \vdots \\ A_{N_o}(n\Delta_f) \end{Bmatrix} = \begin{bmatrix} H_{11}(n\Delta_f) & H_{12}(n\Delta_f) & \cdots & H_{1N_i}(n\Delta_f) \\ H_{21}(n\Delta_f) & H_{22}(n\Delta_f) & \cdots & H_{2MN_i}(n\Delta_f) \\ \vdots & \vdots & \vdots & \vdots \\ H_{N_o1}(n\Delta_f) & H_{N_o2}(n\Delta_f) & \cdots & H_{N_oN_i}(n\Delta_f) \end{bmatrix} \begin{Bmatrix} F_1(n\Delta_f) \\ F_2(n\Delta_f) \\ \vdots \\ F_{N_i}(n\Delta_f) \end{Bmatrix}, \quad (1)$$

$$\text{for } \mathrm{n} = 0, 1, \ldots, N_f.$$

Equation (1) represents a set of N_f system of equations, which are underdetermined for $N_i > N_o$, that is, when there are more input degrees of freedom than there are output degrees of freedom. If this system of equations was not underdetermined, it could be solved for the frequency spectrum of forces that are applied at each discrete input point. For an impact at one location, all but one of these force spectra should be close to zero. Therefore, rather than estimating N_i forces, $N_i - 1$ of which should be very small for the single impact situation being considered, a better estimate of the one force of interest can be found by assuming there is only one force input point. This assumption that a forcing function acts at a single point allows for a set of overdetermined system of equations to be formulated, provided that more than one acceleration response signal is available. If it is known (or assumed) that a force acts at degree of freedom k, the system of equations in (1) becomes:

$$\begin{bmatrix} A_1(0) & A_1(\Delta_f) & A_1(2\Delta_f) & \dots & A_1(N_f\Delta_f) \\ A_2(0) & A_2(\Delta_f) & A_2(2\Delta_f) & \dots & A_2(N_f\Delta_f) \\ \vdots & \vdots & \vdots & \ddots & \vdots \\ A_{N_o}(0) & A_{N_0}(\Delta_f) & A_{N_o}(2\Delta_f) & \dots & A_{N_o}(N_f\Delta_f) \end{bmatrix} =$$

$$\begin{bmatrix} H_{1k}(0) & H_{1k}(\Delta_f) & H_{1k}(2\Delta_f) & \dots & H_{1k}(N_f\Delta_f) \\ H_{2k}(0) & H_{2k}(\Delta_f) & H_{2k}(2\Delta_f) & \dots & H_{2k}(N_f\Delta_f) \\ \vdots & \vdots & \vdots & \ddots & \vdots \\ H_{N_ok}(0) & H_{N_ok}(\Delta_f) & H_{N_ok}(2\Delta_f) & \dots & H_{N_ok}(N_f\Delta_f) \end{bmatrix}$$

$$\begin{bmatrix} F_k(0) & 0 & 0 & \dots & 0 \\ 0 & F_k(\Delta_f) & 0 & \dots & 0 \\ 0 & 0 & F_k(2\Delta_f) & \ddots & 0 \\ \vdots & \ddots & 0 & \ddots & 0 \\ 0 & 0 & 0 & \dots & F_k(N_f\Delta_f) \end{bmatrix}. \quad (2)$$

This overdetermined inverse problem in equation (2) is suitable for solving using least squares methods to minimize the error in the estimates that are derived from each acceleration channel. In this work, the linear least squares best fit of the force estimate is computed by way of the Moore-Penrose pseudoinverse, which is a standard method for solving such problems [**?**]. Abbreviating equation (2) as $\left[A\right] = \left[H_k\right]\left[F_k\right]$, the best fit estimate of the diagonal force matrix is given by $\left[\hat{F}_k\right] = \left[H_k\right]^+\left[A\right]$, where $\left[H_k\right]^+$ is the pseudoinverse of $\left[H_k\right]$. An important note concerning this method of estimating the force spectrum is that while computing the pseudoinverse of large matrices such as $\left[H_k\right]$ is computationally expensive, the pseudoinverse of the matrix is entirely independent from the observed response; therefore, the pseudoinverse can be computed in advance of monitoring a structure for impacts, making it possible to estimate the force spectrum using a matrix product, which is a relatively fast computational task.

While the form in equation (2) is the most compact representation of the inverse problem, the actual form used in the algorithm's implementation differs slightly and allows the estimated force spectrum to be represented by a vector, rather than a large diagonal matrix. This approach saves considerable amounts of memory when the algorithm is implemented. This modified form is obtained by considering equation (1) at one spectral line assuming that only one force is non-zero, as follows:

$$\begin{Bmatrix} A_1(n\Delta_f) \\ A_2(n\Delta_f) \\ \vdots \\ A_{N_o}(n\Delta_f) \end{Bmatrix}_{(N_f x 1)} = \begin{Bmatrix} H_{1k}(n\Delta_f) \\ H_{2k}(n\Delta_f) \\ \vdots \\ H_{N_o k}(n\Delta_f) \end{Bmatrix}_{(N_f x 1)} F_k(n\Delta_f). \tag{3}$$

Abbreviating equation (3) as $\left\{A(n\Delta_f)\right\} = \left\{H_k(n\Delta_f)\right\} F_k(n\Delta_f)$, the best fit estimate of the force at the nth spectral line is written as:

$$\hat{F}_k(n\Delta_f) = \left\{H_k(n\Delta_f)\right\}^+ \left\{A(n\Delta_f)\right\}. \tag{4}$$

Combining all equations in the form of equation (4) for $n = 0, 1, 2, \ldots, N_f$ into one equation yields the form that is used in the actual implementation of this algorithm:

$$\begin{Bmatrix} \hat{F}_k(0) \\ \hat{F}_k(\Delta_f) \\ \hat{F}_k(2\Delta_f) \\ \vdots \\ \hat{F}_k(N_f\Delta_f) \end{Bmatrix} = \begin{Bmatrix} \left\{H_k(0)\right\}^+ \left\{A(0)\right\} \\ \left\{H_k(\Delta_f)\right\}^+ \left\{A(\Delta_f)\right\} \\ \left\{H_k(2\Delta_f)\right\}^+ \left\{A(2\Delta_f)\right\} \\ \vdots \\ \left\{H(N_f\Delta_f)\right\}^+ \left\{A(N_f\Delta_f)\right\} \end{Bmatrix}. \tag{5}$$

2.3 Force Location Identification Theory

While the estimation of a force spectrum at a known input location using training data and response measurements, as presented above, is a straightforward calculation, the problem of identifying the location at which an unknown force acts is considerably more challenging. Several methods exist in literature for force estimation method that are similar to the method presented here ([13, 41, **?**]). The fundamental difference between these similar impact identification methods and the technique presented here is the algorithm for estimating the location of the unknown force. In addition to the similarities in the method of estimating the input force spectrum, each of the algorithms considered begins with the same first step: to calculate the estimated force spectra assuming that the force acted at each of the possible input locations. After this step, N_i force spectra have been estimated, all but one of which is a numerical solution to an inverse problem that does not correspond to the actual physical event that occurred. The entropy-based impact location identification method is the way that we determine which force estimate most likely corresponds to the actual impact location.

The method used for estimating the forcing function input location is the entropy-based algorithm. This algorithm attempts to solve the problems associated with implementing past methods on large, non-homogeneous structures. In addition, this method is much more easily transferred to various structures than previous methods, because only a few parameters must be modified to suit a particular structure.

While the previous related methods discussed above considered the force estimates in the frequency domain, this method instead analyzes the time-histories of the force estimates, which are generated by taking the inverse discrete Fourier transforms of the estimated force spectra. By transforming the estimates into the time domain, one of the key weaknesses of previous methods, the need to identify a specific frequency band of interest, is eliminated. The time domain representation of the signal combines all frequency components together; therefore, the entire bandwidth of the measurement is considered at once. Realistic force histories are identified by characterizing how well force time histories correspond to the assumption of an impulsive forcing function.

Entropy in information theory, as defined by Shannon [50], is the key quantity that will be used as a discriminant between force histories that correspond to impact events and those that are the numerical solution to a non-physical problem. While entropy in thermodynamic applications is commonplace, its application in information theory to mechanical force estimation is new, so an explanation of the meaning of and reasoning behind entropy is given here. This explanation is not a rigorous proof, but rather enough to motivate and understand its application in this work. For a rigorous development of entropy and its use in information theory, see [50].

To begin the explanation of entropy in information theory, information as a quantity must be understood. Information is generally regarded as an abstract idea and is evaluated qualitatively; however to serve a practical purpose in calculations, it must be quantified. In this sense, information is quantified by the number of bits that are required to fully describe that information. For example, consider a series of coin tosses. One coin toss can be directly represented by one bit, by representing heads as a 1, and tails as a 0, for example. So for one coin toss, the outcome of one trial, which has 2 possibilities, can be represented by one bit. Similarly, if there were three coin tosses, there would be $2^3 = 8$ possible outcomes, and three bits would fully describe the particular sequence, so there would be three bits of information in three coin tosses. In a general sense, if there are N possible outcomes of a set of trials, the amount of information given by those trials, I, in bits, is:

$$I = log_2(N). \tag{6}$$

Clearly, this definition matches the expectation from the coin toss example, as the number of possibilities in n coin tosses is 2^n, so the amount of information in n coin tosses is $log_2 2^n = n$ bits. Rather than considering the total amount of information in a set of data, the average amount of information per element in that set, defined as H, could be considered:

$$H = \frac{I}{n}. \tag{7}$$

This measure of information per sample is defined as entropy. In the case of the fair coin toss, the entropy of that process would be 1 bit, which is consistent with expectations, because 1 bit is used to represent each toss. Entropy in this sense is the means of identifying the force-time history that best corresponds to an impulsive force. To explain the way that entropy is calculated in the case of evaluating recreated force-time histories, a useful example is a set of n tosses of an unfair coin, which has a probability p_1 of heads and a probability $p_2 = 1 - p_1$ of tails, where in general $p_1 \neq 0.5$. Assuming a suitably large number of coin tosses, n, the number of occurrences of heads will be given by $m = p_1 n$. While there were $N = 2^n$ possible outcomes of n tosses of a fair coin, the number of possible outcomes of n tosses of this unfair coin is given by:

$$N = \binom{n}{m} = \frac{n!}{m!(n-m)!}. \tag{8}$$

From the previous definition of information, the amount of information in this set of trials is given by:

$$I = log_2(N) = log_2\binom{n}{m} = log_2(\frac{n!}{m!(n-m)!}). \tag{9}$$

Writing this expression for information in terms of the base e rather than 2 and re-arranging, equation (9) can be written as:

$$I = \frac{1}{ln(2)}(ln(n!) - ln(m!) - ln((n-m)!)). \tag{10}$$

Using Sterling's approximation for the natural logarithm of a factorial, $ln(n!) \approx nln(n) - n$ for n very large, equation (10) becomes:

$$I = \frac{1}{ln(2)}(nln(n) - mln(m) - (n-m)ln(n-m)). \tag{11}$$

After straightforward algebra, which is omitted for brevity, and returning to logarithms of the base 2, equation (11) is written as:

$$I = -mlog_2(\frac{m}{n}) - (n-m)log_2(\frac{n-m}{n}). \tag{12}$$

Equation (12) is now written in terms of probabilities p_1 and p_2, giving the final expression for information:

$$I = -np_1log_2(p_1) - np_2log_2(p_2). \tag{13}$$

Finding the average information per toss gives the entropy of the process as follows:

$$H = -p_1log_2p_1 - p_2log_2p_2. \tag{14}$$

Plotting the entropy as a function of probability heads, as in Figure 5, helps to explain how entropy changes based on the characteristics of the underlying process. The entropy is maximized when both events are equally likely, where the entropy is 1 bit, as expected from the previous discussion of a fair coin toss. When there is less uncertainty in the outcome, that is, either heads or tails is more likely to occur, the entropy is less. At the extremes, if the probability of heads approached 100% or 0%, the entropy would be zero. This result makes sense because in either of these cases, with a knowledge of the probability beforehand, no information is gained by each toss of the coin. The outcome of every trial was already known.

Two important characteristics of entropy in general can be drawn from this simple example of two possible outcomes. In all cases, the entropy is maximized when each of k possible outcomes is equally likely, where entropy approaches a maximum value of $H_{max} = log_2(k)$. Second, the minimum entropy approaches zero as the probability of one possible outcome approaches 1.

While the simple example of two possible outcomes is a useful example, it is not sufficient to characterize the force signals of interest. In more practical cases, there exists more than two possible outcomes. The form of entropy in the case of two outcomes, as in equation (14), extends to the case with k possible outcomes, each of which has a probability of p_i, as follows:

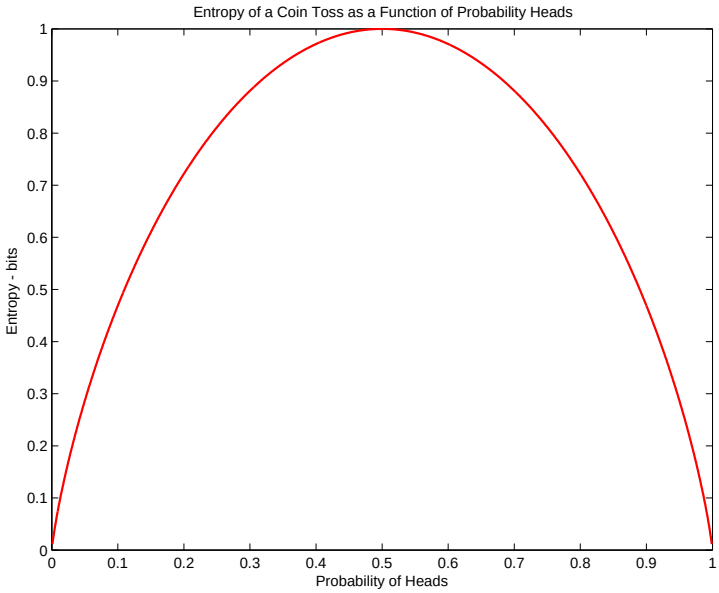

Figure 5: Entropy For A Set Of Unfair Coin Tosses As A Function Of The Probability Of Heads.

$$H = \sum_{i=1}^{k} -p_i log_2 p_i. \tag{15}$$

In this application, equation (15) is implemented to find the entropy of a recreated force signal by dividing the signal into a set number of equally spaced bins, and then finding the number of samples that fall into each bin. These frequencies of occurrence are divided by the total number of samples to give probabilities that the signal falls into each bin range. The entropy is then calculated according to equation (15). To illustrate the process, we consider two example signals, each consisting of ten samples that range in value from 0 to 1. These signals are intended to be a simple example of how a signal that consists of just one pulse has a lower entropy than one that is more random. Five bins will be used to find the entropy of each of the signals, which are given in Table 1. Table 2 shows the results at each step of the entropy process, as well as the final value. The probability of the signal falling into each bin is calculated, and then the contribution to the entropy total is listed for each bin. Finally, the values are summed to find the total entropy of each signal. In this example, the simple pulse signal has an entropy of 0.47 bits, while the random signal has an entropy of 2.32 bits. While this is a somewhat exaggerated example, it illustrates the trend that the most ordered recreated force time histories which best match expectations of a simple pulse will have the lowest entropy value.

Table 1: Two Simple Example Signals, Used To Represent A Signal With A Single Pulse And One That Is More Random.

	Values									
Signal 1	0.0	0.0	0.0	0.0	1.0	0.0	0.0	0.0	0.0	0.0
Signal 2	0.75	0.17	0.3	0.54	0.37	1.0	0.7	0.9	0.0	0.58

Table 2: The Entropy Calculation Process Is Demonstrated For Two Simple Example Signals.

	Signal 1			Signal 2		
Bin	Count	p_i	$-p_i log_2 p_i$	Count	p_i	$-p_i log_2 p_i$
0.00-0.19	9	0.9	0.137	2	0.2	0.4644
0.20-0.39	0	0	0	2	0.2	0.4644
0.40-0.59	0	0	0	2	0.2	0.4644
0.60-0.79	0	0	0	2	0.2	0.4644
0.80-1.00	1	0.1	0.3322	2	0.2	0.4644
Total	10	1	0.469	10	1	2.322

2.4 Impact Identification Uncertainty Quantification

The original use of impact force estimate entropy was exclusively for identifying the most likely impact location by comparing the entropy value with those of other impact force estimates originating from the same impact event. We have discovered that the entropy of the selected impact force estimate can be further used to evaluate the quality of the impact force estimate, and therefore better quantify the uncertainty of the impact force estimate. Because the entropy of the impact force estimate is directly related to how impulsive that force estimate is, the entropy for highly accurate force estimates tends to be lower than that of lower quality estimates. Therefore, by considering the entropy of the final impact force estimate, the uncertainty associated with that estimate can be evaluated in real time, giving an immediate indication of the confidence in that estimate.

To understand how the entropy of the impact force estimate is indicative of the uncertainty of that estimate, it is worthwhile to consider the possible sources of force estimation error. There are a number of potential sources of error in impact identification, ranging from those related to the measurement setup to those violating the assumptions behind the impact identification approach. The five most significant potential issues are as follows:

1. Inaccurate impact location estimate

2. FRF model error

3. Response measurement error

4. Structural nonlinearities

5. Bandwidth of force estimate exceeds that of model

As explained in Section 2.2, the impact load estimation technique is based on deconvolution of a response signal with the impulse response function of the structure relating the response to the force at a particular location. Errors in either the impulse response used for inversion or the measured response signal will cause errors in the force estimate. The impulse response can be incorrect for a few reasons; the impulse response of the structure when the impact occurs may have changed between when IRFs were estimated, or the estimation of the IRFs may have been incorrect as a result of measurement or experimental error.

The impact identification algorithm assumes that the impact occurs at one of a predefined finite set of potential impact locations. Depending on the density of the training data grid, this may not be an adequate assumption, and the force magnitude estimation may have significant error if the actual impact location is not coincident with a training data grid point. To examine how this situation affects the impact force estimate and the entropy thereof, a simplified example will be considered with one response measurement at point a and an impact force occurring at point b. The impulse response of the structure between points a and b is known, and is abbreviated h_{ab}. The response measurement is denoted x_a, the impact force is denoted f_b. In addition, there is another grid point labeled c, which represents another grid point with training data established. This measurement scenario is illustrated in Figure 6, and Figure 7 is a block diagram for this example.

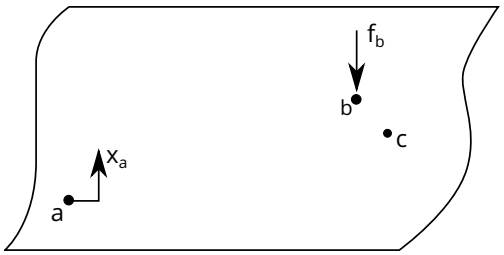

Figure 6: Diagram Of Example Impact Identification Scenario

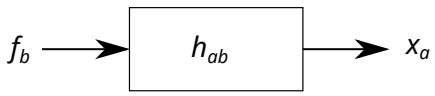

Figure 7: Block Diagram For Single Input, Single Output Example System

The response in this example is equal to the convolution of the impact force with the impulse response function between points a and b, as shown in the following equation.

$$x_a(t) = f_b(t) * h_{ab}(t) \tag{16}$$

Taking the Fourier transform of (16), and noting that convolution in the time domain is equivalent to multiplication in the frequency domain, (16) becomes:

$$X_a(j\omega) = F_b(j\omega)H_{ab}(j\omega) \tag{17}$$

where $H_{ab}(j\omega)$ is the frequency response function between points a and b, $X_a(j\omega)$ is the response spectrum, and $F_b(j\omega)$ is the force spectrum.

Rearranging (17), the inverse force estimation problem can be solved by simple division:

$$F_b(j\omega) = \frac{X_a(j\omega)}{H_{ab}(j\omega)} \tag{18}$$

The estimated impact force in the time domain is then:

$$f_b(t) = \mathscr{F}^{-1}\left(\frac{X_a(j\omega)}{H_{ab}(j\omega)}\right) \tag{19}$$

Now we consider a scenario with an impact at point b and an output at point a, just as before, but where the force is assumed (in error) to have occurred at point c. Following the same approach as before, the force spectrum would be estimated as follows:

$$\hat{F}_c(j\omega) = \frac{X_a(j\omega)}{H_{ac}(j\omega)} \tag{20}$$

Likewise, the force time history would be estimated as:

$$\hat{f}_c(t) = \mathscr{F}^{-1}\left(\frac{X_a(j\omega)}{H_{ac}(j\omega)}\right) \tag{21}$$

Clearly, if $H_{ac}(j\omega) \neq H_{ab}(j\omega)$,then the estimated force, $\hat{f}_c(t)$, is not the same as the actual force, $f_b(t)$, so there is some error in this force estimate. To understand how the force estimate in

this situation relates to the actual force input into the system, (17), can be rearranged as follows:

$$\hat{F}_c(j\omega) = (\frac{X_a(j\omega)}{H_{ab}(j\omega)})(\frac{H_{ab}(j\omega)}{H_{ac}(j\omega)}) \tag{22}$$

Substituting (18) into (22) relates the estimated force spectrum to the true input force spectrum:

$$\hat{F}_c(j\omega) = F_b(j\omega)(\frac{H_{ab}(j\omega)}{H_{ac}(j\omega)}) \tag{23}$$

The ratio of frequency response functions in (23) is equivalent to the transmissability between points b and c, which is the ratio of the response spectra of those points, and is denoted $T_{bc}(j\omega)$. Using this notation gives the simple relationship between the estimated force and the true input force:

$$\hat{F}_c(j\omega) = F_b(j\omega)T_{bc}(j\omega) \tag{24}$$

Noting that multiplication in the frequency domain is equivalent to convolution in the time domain, the estimated impact force time history can be related the true impact force time history and the impulse response of the transmissibility, denoted $t_{bc}(t)$:

$$\hat{f}_c = f_b(t) * t_{bc}(t) \tag{25}$$

The above equation shows that the estimated force time history is like the response to a dynamic system characterized by the transmissibility impulse response rather than a conventional impulse response function. If the transmissibility is unity for all frequencies (that is, if the frequency response function of the system when the impact occurs is identical to the estimated frequency response function from training data), then the inverse Fourier transform of that transmissibility would simply be a dirac delta function, which would lead to the estimated force being identical to the true force, as would be expected in a system with no errors. If, on the other hand, the transmissibility is not unity for all frequencies, the impulse response of that transmissibility function will contain oscillations, which will lead to a force estimate which contains oscillations that were never present in the actual force. These oscillations will lead to a higher entropy value associated with the force estimate.

This page intentionally left blank.

3 Experimental Impact Identification and Uncertainty Quantification

3.1 Experimental Setup

This impact identification technique was tested on a commercial wind turbine blade. The tested blade had been damaged in a lightning strike, and was delaminated at the tip with a portion of the tip missing, but the portion which was tested was largely undamaged. The blade was fastened at the root of the blade to a steel fixture, and supported towards the end of the blade with nylon straps. Figures 8, 9, and 10 show the damaged blade tip, root boundary condition, and the second blade support, respectively.

Figure 8: Tip Damage on Wind Turbine Blade

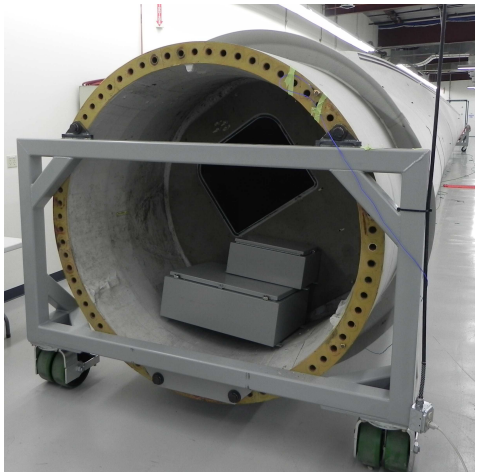

Figure 9: Steel Support At Blade Root

Figure 10: Nylon Strap Supporting Blade Towards The Tip

Five tri-axial accelerometers were mounted to the blade to test the influence of sensor placement on the accuracy of impact identification. The locations of these sensors are shown in Figure 11, along with the number assigned to each. Accelerometer 1 is a PCB 356T18, an ICP triaxial accelerometer with nominal sensitivity of 1000mV/g. Accelerometers 2-5 are Silicon Designs 2460-050 DC coupled peizoresistive triaxial accelerometers with nominal sensitivities of 80mV/g. The relevant sensor information is summarized in Table 3.

Table 3: Accelerometers Used For Impact Identification Study

#	Manufacturer	Model	Nominal Sensitivity	Type	DAQ Coupling
1	PCB	T356B18	1000mV/g	Piezoelectric	AC
2	Silicon Designs	2460-050	80mV/g	Piezoresistive	DC
3	Silicon Designs	2460-050	80mV/g	Piezoresistive	DC
4	Silicon Designs	2460-050	80mV/g	Piezoresistive	DC
5	Silicon Designs	2460-050	80mV/g	Piezoresistive	DC

A grid of 130 impact locations was marked on the section of the blade between the root and the support. The vertical spacing between points was approximately 0.36m, and the horizontal spacing was roughly 0.91m. The impact locations are shown in Figure 11 along with the sensor locations.

To create the frequency response function model of the blade, modal impact testing was carried out using a 5.5kg modal sledge hammer, model PCB 086D50, with a soft rubber tip. The modal impact hammer used is shown in Figure (12). Peak force amplitude for these impacts ranged from 542.2lbf to 2469.3lbf, with a mean value of 1205.4lbf and a standard deviation of 371.5lbf.

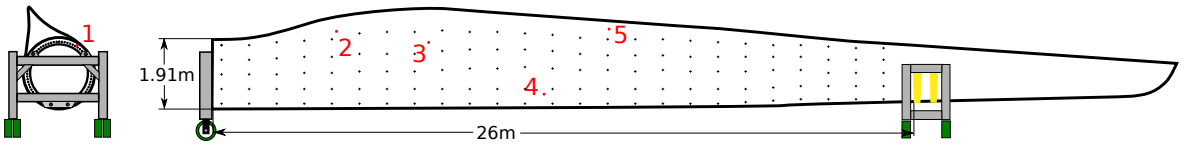

Figure 11: Illustration Of The Blade With Approximate Dimensions, Sensor Locations (Enumerated In Red), And Impact Locations (Marked In Black)

The bandwidth of excitation, as measured by the first frequency where the amplitude of the force spectrum drops to one tenth the maximum amplitude, ranged from 101.5Hz to 281.5Hz, with a mean bandwidth of 174Hz, and a standard deviation of 31.5Hz. Testing was conducted with ten impacts per point, sampled at 2560Hz for a duration of 2 seconds per impact. Frequency response functions were estimated with the H1 estimator.

Figure 12: Modal Sledge Hammer Used For Impact Testing

To test impact identification accuracy, a validation data set was collected with two impacts per point. The impact identification algorithm was applied to response data, and the estimated location and impact magnitude were compared to the known values to evaluate performance.

3.2 Impact Identification Accuracy

In order to test the performance of the impact identification algorithm on the blade, the response data from each validation impact was passed through the algorithm, and the estimated location and maximum force level was recorded. Two key metrics were used to evaluate the accuracy of the estimate: 1) the location identification accuracy, that is, how many of the validation impacts were correctly located, and 2) the magnitude of the peak force error, that is, the absolute value of

the difference between the estimated and measured peak force relative to the measured peak force value.

To evaluate how sensor configurations affected the impact identification accuracy, the data from each of the five accelerometers were used individually to perform these validation simulations. Although the data for these sensors was collected simultaneously, only one sensor is used at a time in these validation tests. Accuracy is evaluated when data from all three measurement directions are used, when data from two of the three measurement directions are used, and when data from a single measurement direction are used.

The results of the validation simulation using all three response channels per sensor are summarized in Table 4. Regardless of the sensor location, 100% of impacts were located to the correct grid point. The accuracy of the impact force magnitude estimates was also fairly consistent between sensor locations. The peak force identification error was biased towards underestimating the peak magnitude of the impact force by an average of 0.68%. The fifth sensor, which was placed the furthest towards the blade tip and closest to the trailing edge, performed the best of the tested locations. The force estimates using the fifth sensor had a median error of 3.3%, with 75% of the impact forces estimated within 5.6% of the true peak force value, and a maximum error of 21.2%. The sensor with the lowest force accuracy was the fourth sensor, which was located closer to the root of the blade and close to the leading edge of the blade. The force estimation error for the fourth sensor had a median value of 4% and a maximum error of 35.8%.

Table 4: Impact Identification Performance Using Each Triaxial Accelerometer

	Location	Magnitude of Peak Force Identification Error				
Sensor	Identification	Percentile			Max	Max
Number	Accuracy	25^{th}	50^{th}	75^{th}		
1	100%	1.74%	4.08%	6.39%	4.77%	27.91%
2	100%	1.71%	3.76%	6.38%	4.86%	30.74%
3	100%	1.79%	4.20%	6.61%	4.84%	25.58%
4	100%	1.99%	4.05%	6.83%	4.94%	35.80%
5	100%	1.60%	3.32%	5.57%	4.17%	21.17%

From these results, the force accuracy shows no significant dependence on the distance from the sensor. Figure 13 is a scatter plot of the force error plotted against distance from the sensor, showing the results of validation tests using each of the available sensors. This plot illustrates the independence of the force accuracy on the distance from the sensor, even for very large distances. Most of the largest force estimation errors that were observed were at locations relatively close to the sensor, but this fact is probably in part due to the larger number of points that are an intermediate distance from the sensor than those very distant. Other impact force identification techniques, such

as the method presented in [49], have shown a linear increase in error with distance from the sensor, so the fact that distance and accuracy are largely uncorrelated in this instance is significant.

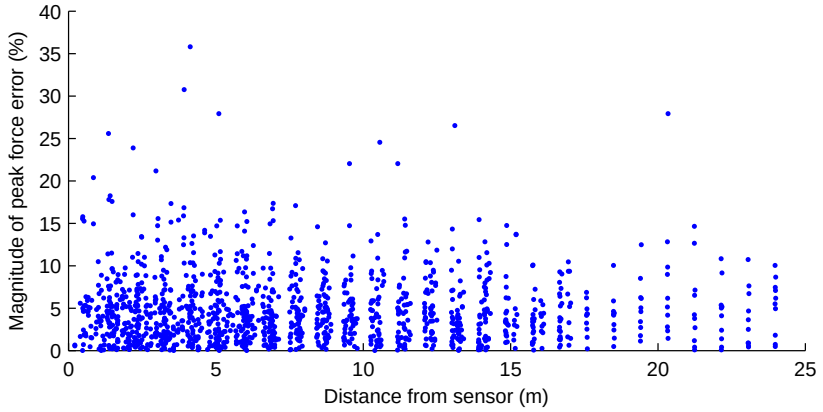

Figure 13: Force Estimation Error Vs. Distance From Sensors For All Combinations Of Sensor And Impact Location

The same type of validation test was repeated with only two of the three response directions used, with the response data in the axial direction ignored. Using this subset of the data produces results very similar to those when all three response channels per sensor are used. The results are detailed in Table 5. Most of the mean errors are marginally higher than when using all three channels, but the median errors and maximum errors are mostly lower. Based on these results, a bi-axial accelerometer could be used just as effectively as a tri-axial accelerometer, even on very large structures. When using a single response channel, impact location performance was generally acceptable, with accuracy greater than 95% for all tested sensor locations and directions. However, the force estimation accuracy was significantly lower than the bi-axial and tri-axial test cases, and these measurement configurations would likely be more sensitive to measurement errors, because the inverse problem being solved is not overdetermined. Table 6 summarizes these results when using a single measurement channel.

Table 5: Impact Identification Performance Omitting Data in the Axial Direction

	Location	Magnitude of Peak Force Identification Error				
Sensor	Identification	Percentile			Mean	Max
Number	Accuracy	25^{th}	50^{th}	75^{th}		
1	100%	1.87%	3.91%	6.58%	4.81%	28.13%
2	100%	1.63%	3.76%	6.37%	4.84%	30.29%
3	100%	1.81%	4.24%	6.59%	4.89%	25.44%
4	100%	1.95%	3.97%	6.73%	4.92%	35.72%
5	100%	1.57%	3.26%	5.54%	4.19%	21.06%

Table 6: Impact Identification Performance Using Individual Measurement Directions (X :chordwise, Y:spanwise, Z:normal)

Sensor & Direction		Location Identification Accuracy	Magnitude of Peak Force Identification Error				
			Percentile			Mean	Max
			25^{th}	50^{th}	75^{th}		
1	X	100%	1.94%	4.19%	6.88%	4.95%	25.75%
	Y	100%	1.79%	3.94%	7.39%	5.11%	29.26%
	Z	99.23%	2.47%	4.26%	7.37%	5.35%	30.39%
2	X	99.23%	1.76%	4.27%	7.49%	5.17%	30.87%
	Y	97.69%	2.12%	4.59%	9.78%	7.32%	114.46%
	Z	100%	1.67%	3.71%	6.51%	4.95%	29.92%
3	X	99.62%	1.67%	4.15%	6.78%	4.84%	26.18%
	Y	95.77%	2.65%	6.77%	11.36%	11.06%	343.04%
	Z	100%	2.05%	4.31%	6.87%	5.07%	26.06%
4	X	100%	1.66%	4.05%	7.02%	4.95%	34.02%
	Y	99.23%	2.30%	4.64%	8.91%	6.62%	96.45%
	Z	100%	1.87%	4.17%	6.63%	5.01%	37.84%
5	X	100%	1.85%	3.78%	6.68%	4.74%	26.35%
	Y	97.31%	2.29%	4.73%	8.22%	6.44%	67.93%
	Z	99.23%	1.51%	3.64%	6.31%	4.62%	43.46%

The validation simulation results show that entropy of the estimated force time histories is an effective measure to discriminate between the force at the actual impact location and the other erroneous force estimates. When using two or three response channels, every impact was correctly located, so the entropy value corresponding to the impact location was always the least. To better evaluate how effective the recreated force entropy is in discriminating between correct and incorrect locations, the recreated force entropy is compared between the actual impact locations and the other incorrect impact locations. The results from all of the three channel validation response simulations were considered, and histograms of the recreated force entropy values for correct and incorrect locations are shown in Figure 14. For this comparison and the following entropy discussion, the signals were discretized to 200 amplitude values. Therefore, a purely random signal would have $log_2(200) = 7.64$ bits of entropy. This comparison of entropy value distributions shows that the recreated force entropy is a very effective discriminator between the correct and incorrect locations. There is very little overlap between the two distributions, the entropy of the incorrect locations is tightly distributed, and the values of the correct location entropy are much lower than those from the corresponding incorrect locations. When entropy values from one impact were considered, the value corresponding to the correct location was always more than 1.5 times the interquartile range of the other entropies, with some values more than 10 times the interquartile range below the other entropy values. This measure indicates that for this set of data, not only is

the entropy for the correct location always lowest, it is always a clear outlier of the distribution.

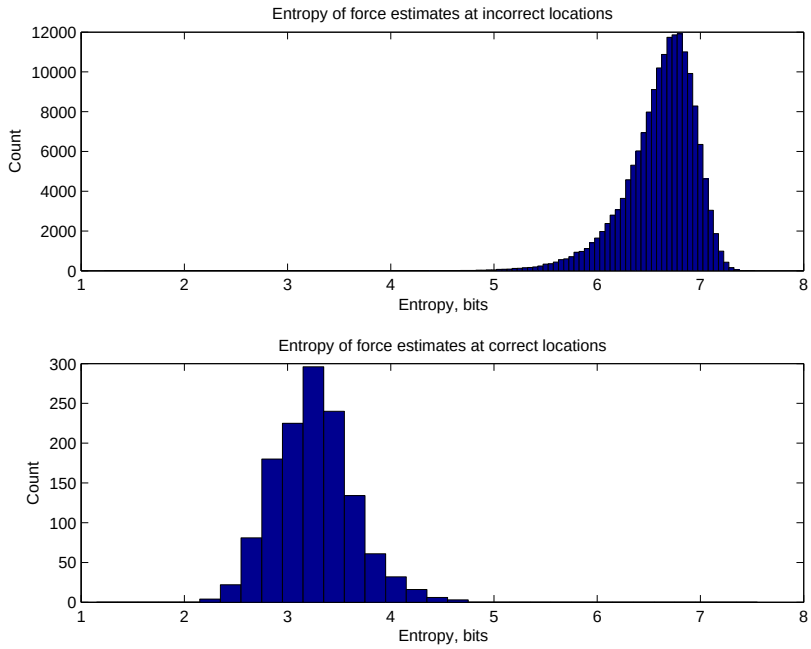

Figure 14: Histograms Showing The Distribution Of Entropy Values For Force Estimates Corresponding To Incorrect Locations (Top) And Correct Locations (Bottom)

3.3 Uncertainty Quantification

Entropy of the recreated force time histories effectively locates impacts because the value characterizes how well the force estimate meets the assumption of an impulsive load. Therefore, noise and error in the force estimate that alters the shape of the recreated force signal would generally contribute to an increase in the entropy of the force estimate. To evaluate the extent that the entropy of the recreated force time history is related to error in the force estimate, the force estimates were split into seven categories according to entropy value. Boxplots of the magnitude of force estimation error were plotted for each of these entropy ranges in Figure 15, along with a histogram showing the frequency of estimates within each of these entropy ranges. Statistical measures corresponding to each of these entropy ranges are detailed in Table 7.

Both the average bias and variance of the force estimation error are monotonically increasing with the entropy value of the estimated force. Both the mean error and standard deviation for the force estimates with entropy greater than four are more than three times the corresponding values for estimates with entropy less than 2.5. This result is important because with an understanding

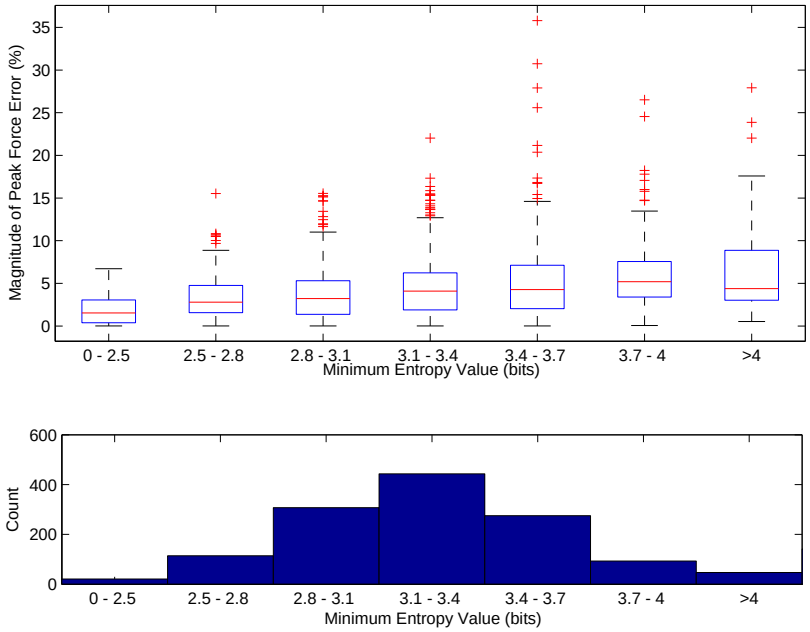

Figure 15: Relationship between impact force identification error and entropy of the force estimate

of how the recreated force entropy and force error are related, the uncertainty in a force estimate could be characterized based on the entropy value for that estimate. Uncertainties based on the entropy value of the force estimate would be more accurate than uncertainty measures based only on the errors of the validation data set as a whole.

Table 7: Peak Force Estimation Error Statistics Corresponding To Estimated Force Entropy

Entropy Range (bits)	Count	Magnitude of Peak Force Error (%)				
		Percentile			Mean	Standard Deviation
		25^{th}	50^{th}	75^{th}		
0 - 2.5	21	0.38	1.54	3.06	2.04	1.93
2.5 - 2.8	114	1.56	2.80	4.76	3.51	2.88
2.8 - 3.1	307	1.38	3.22	5.30	3.97	3.32
3.1 - 3.4	443	1.89	4.09	6.22	4.72	3.64
3.4 - 3.7	275	2.04	4.27	7.13	5.28	4.86
3.7 - 4	93	3.40	5.19	7.56	6.43	5.05
¿4	47	3.03	4.3	8.87	6.97	6.19

To further investigate the quantification of impact load uncertainty based on estimated force entropy, empirical cumulative distributions of the magnitude of impact force estimation error were investigated. These distributions, shown in Figure 16, indicate the increasing uncertainty and higher force estimation error for higher entropy forces. Another important feature of these distributions

is that the distribution based on all force estimates is a poor indicator of the uncertainty of force estimates with high or low entropy values. Categorizing force estimates based on recreated force entropy better characterizes the uncertainty in that force estimate.

When considering all force estimates, 95% of validation tests showed a peak force estimation error of less than 12.6%. In contrast, 95% of estimates with entropy of less than 2.5 bits were accurate within 5.5%, while the same measure was 22% for force estimates with more than 4 bits of entropy. Therefore, the uncertainty for force estimates in the lowest entropy range was significantly overstated by the distribution of all estimates, and the uncertainty for force estimates with the highest entropy was significantly understated by the distribution of all estimates.

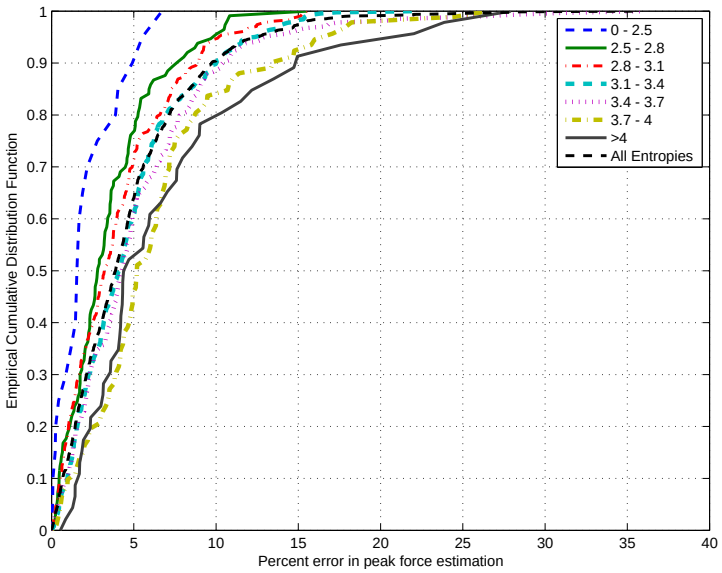

Figure 16: Empirical Cumulative Distributions Of Peak Force Estimation Error For Force Estimates Of Varying Entropy

3.4 Conclusions

The entropy-based impact identification technique presented here was very effective at accurately locating impacts on a large, non-homogenous structure using data from only one sensor. Location identification performance was 100% accurate for all tested sensor locations when using acceleration data from two or three sensor directions, and on average 99.15% accurate when using a single measurement direction.

The measure of recreated force entropy discriminates between force estimates from correct

and incorrect locations very well, with the entropy at the correct location always being a statistical outlier. The value of the minimum recreated force entropy was shown to be a good indication of the uncertainty in the force estimate. Both the bias and variance of the force estimation error monotonically increased with increasing entropy values.

4 Linear Vibration-Based Techniques for Impact Damage Assessment

4.1 Application to Weak Bond Lap Joint Test Specimen

Linear vibration based techniques for nondestructive testing and structural health monitoring identify changes in the structure related to the distribution and magnitude of the mass, stiffness, damping, and boundary conditions of a structure or test sample. Because these techniques do not rely on the presence of a geometric irregularity or imperfection such as a disbond, delamination, or void, they are promising for identifying damage mechanisms which do not present with these features. Weak bonds in composite manufacturing are a significant problem that is still yet to be well understood and identified. Separate work at Sandia National Labs has sought to replicate this phenomenon in test articles which feature weak bonds like those of concern to manufacturers. These weak bonds were implemented on metallic test articles featuring a lap joint in the middle of varying bond strength. Although weak bonds are not the primary area of interest for this work, these test articles offered a good opportunity to evaluate how the vibration properties of the structure can change with subtle damage mechanisms.

Table 8: Summary Of Weak Bond Test Specimen

	% Full Bond Strength	Description
1	100%	Pristine
2	46%	Baking powder 10% coverage with silk screen
3	26%	Grease layer, 0.02mm thick, 100% coverage
4	10%	Baking powder 100% coverage

To test how vibration-based structural health monitoring techniques might work on a sample like these, four test specimen were tested and analyzed. The test samples considered are summarized in Table 8.

Experimental setup

The experimental approach for testing these samples was to first identify the temporal properties of the system, directly at the bond location, and then identify the spatial characteristics of the response of the sample as a whole. To that end, two tests were performed on each sample: a shaker test and a modal impact test.

First, a 7lbf max force modal shaker was attached to the specimen at the bond location with an impedance head measuring the input force and acceleration response. Figure 17 shows the configuration for this test. The specimen was clamped to the table by way of steel supports, with a layer of rubber between the test beam and the steel supports to avoid rattle problems. A temporary mount was attached at the midpoint using Loctite 454 instant adhesive, and the impedance head was fastened to the mount using a threaded stud. The selected forcing function for this test was a sine sweep, with frequency increasing from 10Hz to 1500Hz over the span of two seconds. Data was sampled over the duration of the sine sweep at a rate of 25000Hz. Twenty data sets per sample were collected, and frequency response functions were estimated using the H1 FRF estimator, which minimizes the effect of noise on the response measurements.

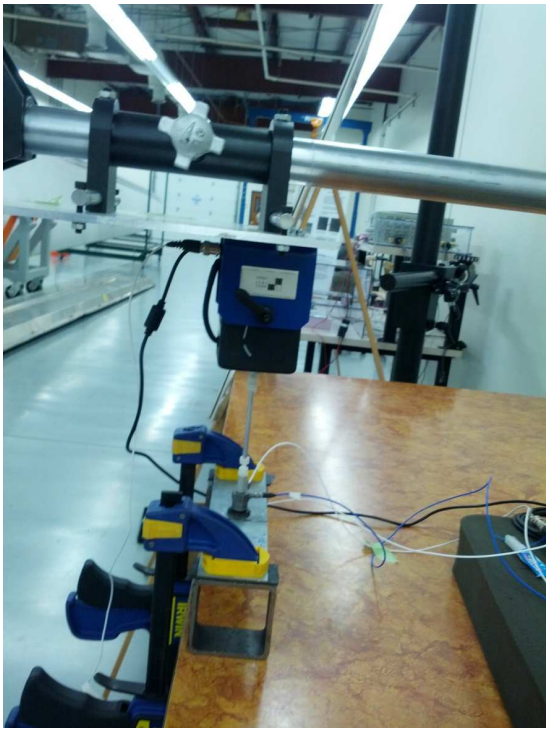

Figure 17: Experimental setup for driving point impedance measurement

After this test was complete, the impedance head was replaced with an accelerometer at the same location, and two additional accelerometers were mounted at the edges of the specimen. All accelerometers used for this test were 10mV/g ICP piezoelectric sensors manufactured by PCB group. A grid of impact locations was marked as shown in Figure 18. A PCB modal impact hammer, model 086C01, with a nylon tip, was used to impact the beam at each of these locations, five times per grid point. The force and response was measured for each of these impacts, and frequency response functions were estimated using the H1 FRF estimator.

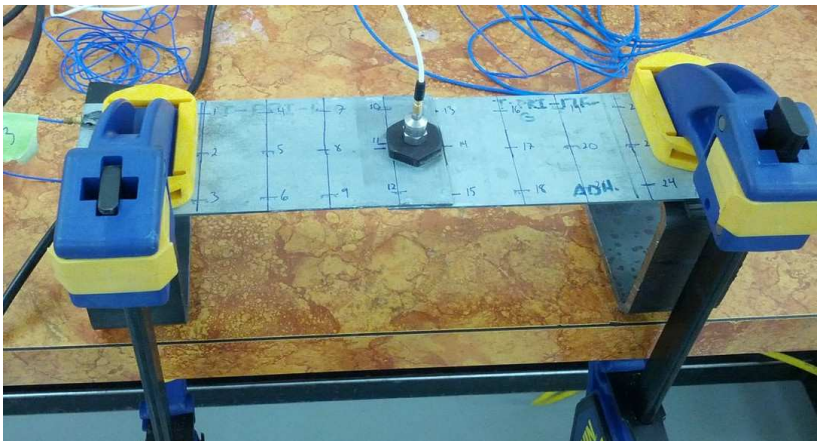

Figure 18: Experimental Configuration For Modal Impact Testing Weak Bond Specimen

Results

Driving point frequency response functions at the lap joint were compared for the four tested specimen, and are shown in Figure 19. These frequency response functions show a number of features which are revealing about the nature of the damage. The low frequency dynamics show very little change between specimen, indicating that the static stiffness of the structure overall is very similar despite the weak bonds. Two natural frequencies are present in the tested frequency range; the first around 150Hz, and the second in the 750-850Hz range. The first natural frequency changes very little between test specimen, but the second natural frequency changes substantially. As the bond strength decreases, this mode decreases in frequency. This behavior is indicative of a reduction in the dynamic stiffness of the specimen at that frequency, and it shows the structural differences between these varying levels of bond strength. The frequency of this mode seems to monotonically decrease with decreasing bond strength. The phase of the frequency response functions around this resonance also indicate that the damping of the weak bond specimen is higher than that of the pristine specimen, as indicated by the slope of the phase curve at the natural frequency, which is inversely proportional to the damping of that mode. Separate work at Sandia determined that this increase in damping was a stronger indicator of weak bonds than shifts in natural frequencies. Another interesting observation is that the amplitude of the frequency response function in the vicinity of this mode shows a strange shape for the 10% and 26% bond strength specimen. This frequency response function shape would not be predicted by a linear model of the structure with a single mode in that frequency range, so this uneven shape could be an indicator of nonlinear dynamic behavior near this resonance.

To further understand the changes in the dynamics between these weak bond test specimen, a

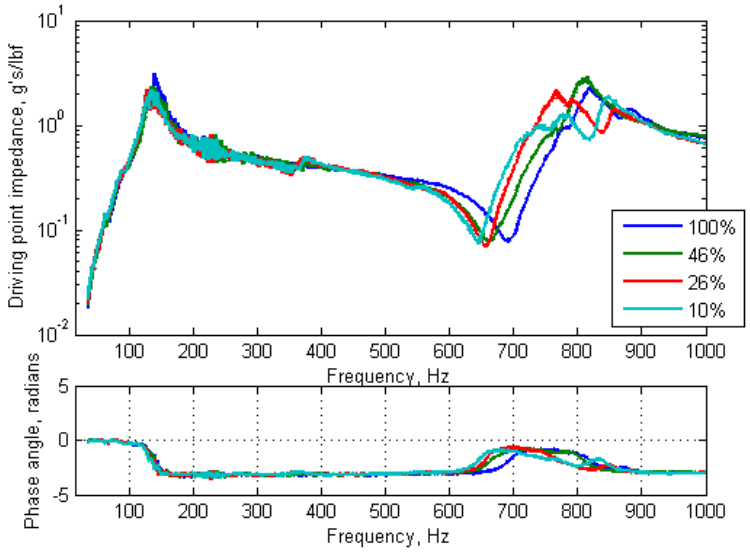

Figure 19: Driving Point FRFs At Bond Location For Several Levels Of Bond Strength

modal decomposition was carried out using the modal impact test data. The set of roving impact hammer frequency response functions were transformed into discrete impulse response functions, and a high order matrix polynomial auto regressive moving average model was fit to the data. The technique used is called Polyreference Time Domain (PTD), because it incorporates data from more than one reference sensor measurements to better estimate the properties of the system. Applying PTD gave modal frequency estimates and modal participation factors. These modal parameters were then used with a high order time domain mode shape estimator to estimate the mode shape associated with each frequency. Model order was increased iteratively until modal parameter estimates converged to stable values.

The mode shape estimates for the 46% bond strength specimen at the two modes seen in the driving point impedance frequency response functions are shown in Figures 20 and 21. As expected, the first mode in the driving point FRFs (133Hz) was seen to be the first bending mode. The adhesive imperfections at the lap joint had little effect on the stiffness for this mode, likely due to the small curvature at the site of the lap joint for this mode, and the small change in static stiffness caused by the adhesive contaminants. The mode which showed the most change was the third bending mode, which was in the 700-900Hz range. For the 46% bond strength test specimen, that mode was at 817Hz. The second bending mode was not observable in the driving point impedance tests because the actuator was directly at the center of the beam, which is a node for the second bending mode.

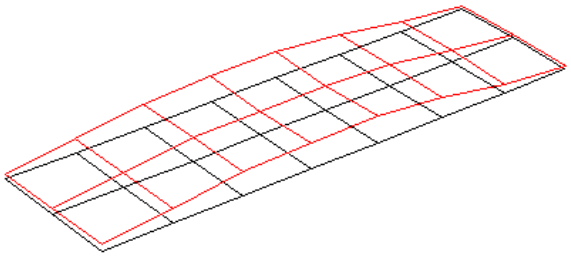

Figure 20: Experimentally Identified Mode Shape Of The 46% Bond Strength Test Specimen For The First Mode At 133Hz

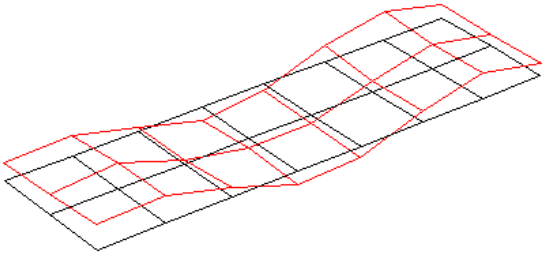

Figure 21: Experimentally Identified Mode Shape Of The 46% Bond Strength Test Specimen For The Third Mode At 817Hz

The implication of these results is that in this instance, the local reduction in stiffness at the center of the beam results in a change in the global vibration properties of the system. With adequate sensor placement (i.e. not at or near a node for the third bending mode), this change in the frequency response of the structure could be sensed by remote sensors, which is promising. By knowing the location of the structural change, remote measurements could be enhanced to more prominently show the changes in this third bending mode. This finding supports the idea of using the impact location estimate to enhance the sensitivity of damage detection techniques. In this instance, if the potential damage area was known to be at the center of the beam, for instance, even modes could be ignored, and modes where significant curvature across the joint were present could be enhanced.

Although these results are promising, it is still important to keep in mind that there are a number of simplifications present in this test which may not generalize to more complex structures, including:

- The beam was a simple metallic beam with low damping, which is ideal for modal analysis and sensing vibration changes.

- The frequency response is modally sparse in the frequency range below 1kHz, so the individual modes are easily distinguished. When there are a number of modes with frequencies in the vicinity of interest, sensing the change becomes more difficult, particularly when the damping for the mode of interest increases.

- The adhesive in this instance was the only material connecting the two parts of the beams, so the stiffness of this adhesive played a major role in the overall stiffness of the structure. When the adhesive is a less prominent structural feature, the changes in the frequency response may be much more subtle. However, many modern construction techniques use bonded joints as very prominent features, so this result is useful for many applications.

4.2 Increasing Sensitivity With Location-Based Filter

To examine the possibility of enhancing the sensitivity of remote measurements to damage at a known location, a simple analytical model representing a structure before and after a damaging event was created. Then, the idea was tested on a composite pressure vessel which was damaged using a drop tower.

Theory and Simulated Example Application

A simple model of a cantilever beam was created using 15 Bernoulli-Euler elements. Two degrees of freedom near the cantilever end of the beam were selected for the input and the output measurements, and the 7th element from the cantilevered end was chosen as the simulated damage location. The reason behind this configuration is that the damaged element is distant from the measured elements, is not at a known node location, and is not bounded by the input and output measurements. The beam with indicated damage, response, and forcing locations is shown in Figure 22.

Mass and stiffness matrices were created for each element, and these mass and stiffness matrices were assembled with boundary conditions taken into account to give the mass and stiffness matrices for the system as a whole. Proportional damping was assumed, and frequency response functions were generated using these mass, stiffness, and damping matrices, assuming that element 2 is the response measurement, element 3 is the forcing location, and element 7 is the one to be damaged. Damage at this location was simulated by reducing the stiffness of that element by 25%, while leaving all other stiffnesses the same. Frequency response functions were calculated before and after the simulated damage was introduced.

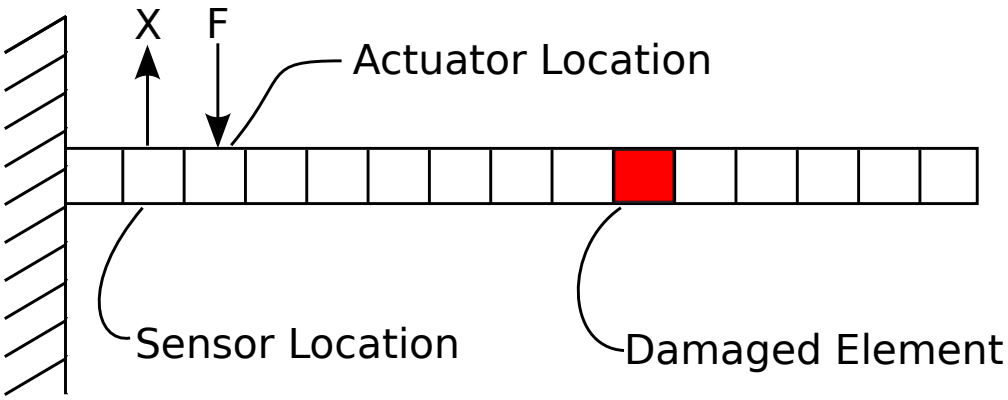

Figure 22: Diagram Of Cantilever Beam Model

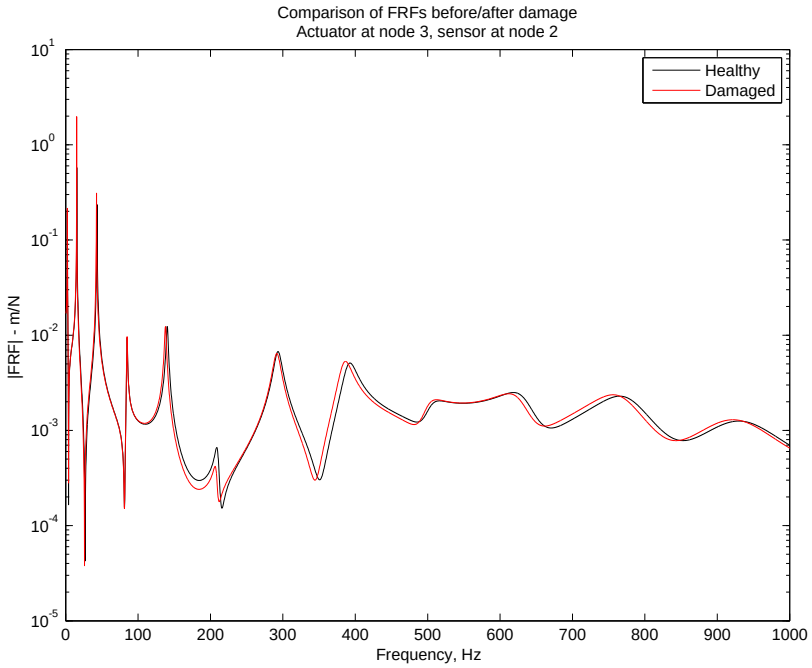

Figure 23: Difference In FRFs Before/After Damage Between The Actuator And Response DOFs

Figure 23 shows the difference in frequency response functions between the second and third element before and after simulated damage. A reduction in some natural frequencies is evident, and the behavior around 200Hz is lower amplitude in the damaged case than the undamaged case. To characterize the overall change in the frequency response functions before and after damage, a damage index was calculated. Denoting the frequency response functions between degrees of

freedom p and q as H^*_{pq}, the damage index was calculated as follows:

$$DI = \sum_{f=0Hz}^{1000Hz} \frac{|H_{23}(j2\pi f) - H^*_{23}(j2\pi f)|}{|H_{23}(j2\pi f)|} \tag{26}$$

To enhance the sensitivity of this method to damage, the frequency response functions after damage were then weighted by the transmissability between the second and seventh degrees of freedom, as measured before the damage was introduced. Had the frequency response functions stayed the same between the two data sets, the frequency response function weighted by the transmissability would be identical to the frequency response between the third and seventh degrees of freedom before damage. Because the damage altered the dynamic response, however, the two measures were significantly different. Figure 24 compares these two frequency response functions. The same type of damage index as in (26) was then calculated as follows:

$$DI = \sum_{f=0Hz}^{1000Hz} \frac{|H_{27}(j2\pi f) - H^*_{23}(j2\pi f) * T_{37}(j2\pi f)|}{|H_{27}(j2\pi f)|} \tag{27}$$

In the above equation, $H^*_{27}(j\omega)$ was estimated by multiplying the updated frequency response function between the second and third degrees of freedom, $H^*_{23}(j\omega)$, by the transmissibility between the third and seventh degrees of freedom before damage, $T_{37}(j\omega)$. This multiplication in the frequency domain is equivalent to a convolution in the time domain, and if this was a set of experimental data, digital filter design techniques would have been used on the impulse response of the transmissibility to reduce numerical issues that could come with implementing this multiplication directly.

The damage indices indicated that weighting by the transmissibility effectively increased the sensitivity to damage. The first damage index indicated a 22.7% change over the range of interest when comparing the FRFs between the sensor and actuator, while the damage index comparing the transmissibility weighted FRFs indicated a 32.1% change. This shows that for this simple model, a 41% increase in the sensitivity to damage is possible by taking into account a known (or assumed) location of damage.

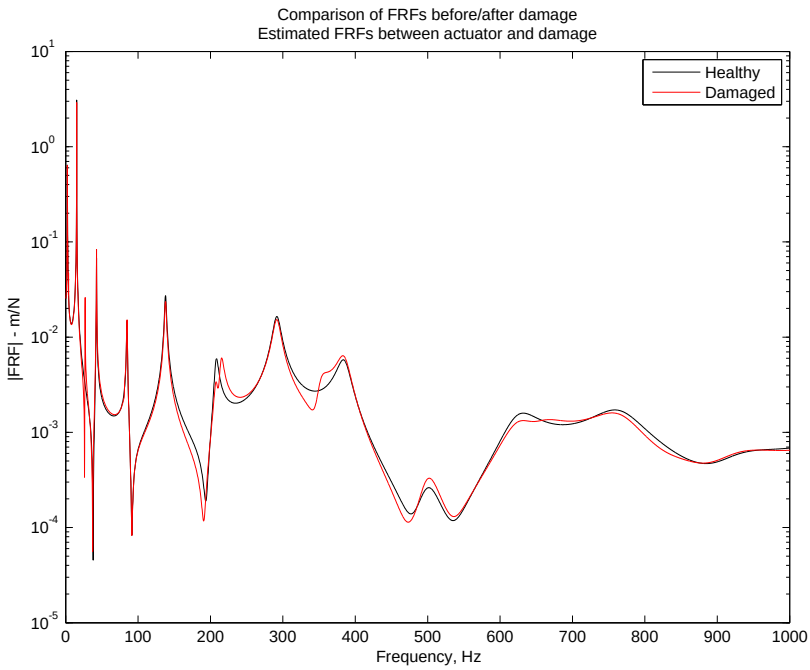

Figure 24: Comparison Of FRFs Before/After Using Synthesized FRFs Between The Actuator And The Damage Degrees Of Freedom.

Application to composite pressure vessel

To test a more realistic structure, a composite pressure vessel was tested in an attempt to replicate the results seen in the analytical example. To experimentally realize these measurements, modal impact testing and sine sweep actuator testing were conducted before and after impacting the pressure vessel with an 80ft-lbf energy level impact from a drop tower with a 0.5" steel hemispherical tip. The drop tower test was able to create a very limited amount of visible damage, but this energy level and boundary condition under the drop tower was known to create significant damage on other identical pressure vessels in the past.

Figure 25 shows the pressure vessel which was tested, supported from above by a flexible bungee cord, with a piezoelectric disc actuator mounted towards the bottom, and an accelerometer mounted towards the top. The grid points which were impacted are also enumerated in the picture.

When the canister was drop tested, the actuators were removed and replaced with shock accelerometers in order to protect the actuators. Figure 26 shows the pressure vessel under the drop tower. The point to be impacted is directly between the two bungee cords, which hold the canister firmly against a steel support.

Figure 25: Composite Pressure Vessel Tested, With Accelerometer And Actuator Attached

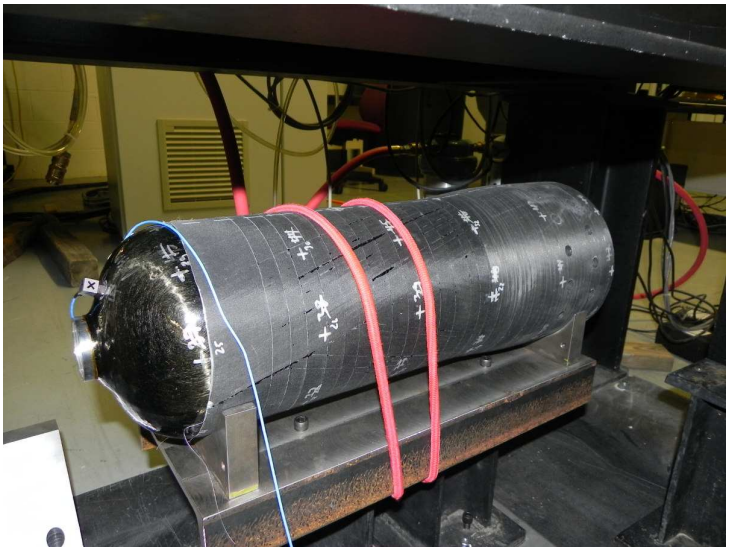

Figure 26: Composite Pressure Vessel Under The Drop Tower To Create Damage

Figure 27 shows the estimated frequency response functions before and after damage with transmissibility weighting (top) and without (bottom). As in the analytical example, small shifts in the frequency response functions in the original measurements become distinct peaks when

weighted by transmissibility. However, significant challenges are seen in this data set which were not in the more simple analytical beam model. Depending on the frequency range over which the damage index was calculated, the weighting could have either increased or decreased the sensitivity to damage. The frequency range which produced the most significant change in the frequency response would not necessarily be the same for each possible damage location, so simply calculating a damage index over an ideal range would be somewhat misleading; the damage sensitivity may be higher in this instance, but lower in another.

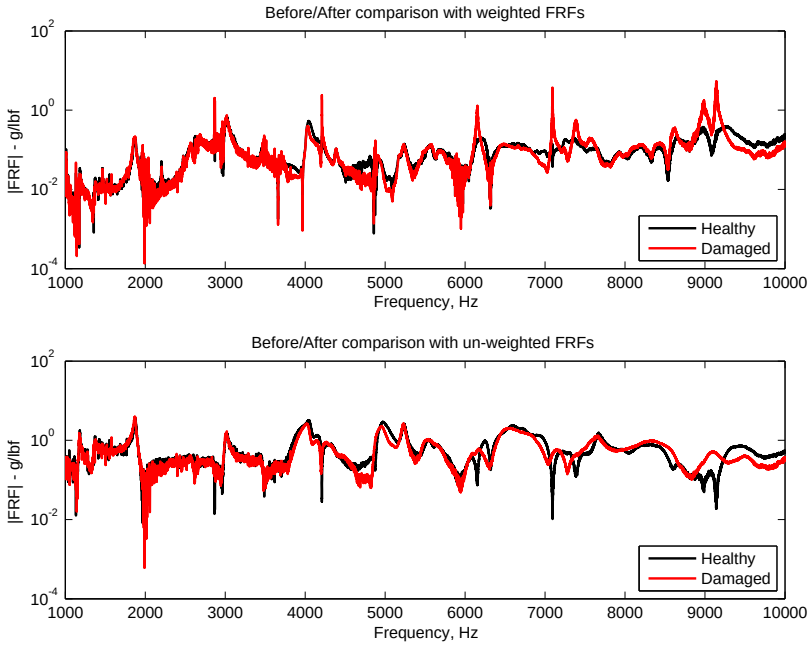

Figure 27: Comparison Of FRF Amplitude Before And After Damage With And Without Transmissibility Weighting.

In addition to the challenges in selecting an appropriate frequency range, when applying the transmissability filter to enhance the changes in the frequency response functions before and after damage, problems occurred at the anti-resonances of the frequency response function between the actuator and sensor. To investigate the cause and potential solutions to this problem, the frequency response functions were expressed in several forms. The first is a polynomial form in the Laplace domain, with the numerator of a frequency response function $H_{pq}(s)$ denoted $B_{pq}(s)$, and the denominator of all frequency response functions of the system denoted as $A(s)$. The relevant degrees of freedom in this discussion are d - the potential damaged location, f - the forcing location, and a - the accelerometer location. Frequency response functions with the $*$ superscript are those measured after a potentially damaging impact, and those without the asterisk superscript are measured before the potentially damaging impact. The approach is to estimate the frequency

response between the potentially damaged location and the sensor location by forcing the function by the actuator and using a ratio of transmissabilities measured beforehand:

$$H^*_{ad} \approx \frac{H_{ad}}{H_{af}} H^*_{af}$$

Expressing the transfer functions as the ratio of polynomials as discussed above, this becomes:

$$H^*_{ad} \approx \frac{B_{ad}(s)}{B_{af}(s)} \frac{B^*_{af}(s)}{A^*(s)}$$

The resonances of the system are the roots of the denominator polynomial, $A^*(s)$, and are universal across all degrees of freedom, while the anti-resonances are local properties of the system and are the roots of the numerator polynomial, $B_{pq}(s)$. The anti-resonances between the forcing and response degrees of freedom (the roots of $B_{af}(s)$) are not of interest for damage detection, but interfere with the results if $B_{af} \neq B^*_{af}$; any root of $B_{af}(s)$ that is not completely canceled by a root of $B^*_{af}(s)$ causes a situation where there is a division by a number very close to zero. This near divide by zero problem causes a significant spike in the recreated frequency response function between the damage and sensor location. While this change does result in a significant increase in the difference before and after damage, the problem is that the spike is not necessarily a result of the damage, and would be present even if the change in the system is completely unrelated to damage (e.g. environmental changes, subtle boundary condition changes, etc.).

An example of this problem in experimental data is shown in Figure 28. The large spikes in the recreated frequency response function (top) are a result of this division by zero problem. The blue vertical lines in this figure are used to show how the anti-resonances of the directly estimated frequency response functions (bottom) correspond to the large spikes in the recreated frequency response functions.

4.3 Conclusions

The linear vibration based damage identification techniques presented here show that this approach is capable of detecting structural abnormalities relative to a known healthy baseline, but the application of these techniques can present significant challenges. The weak bond test specimen show that flaws which do not decrease the static stiffness of the structure can be detected by reductions in the dynamic stiffness and increase in damping, and that the spatial nature of the flaw determines

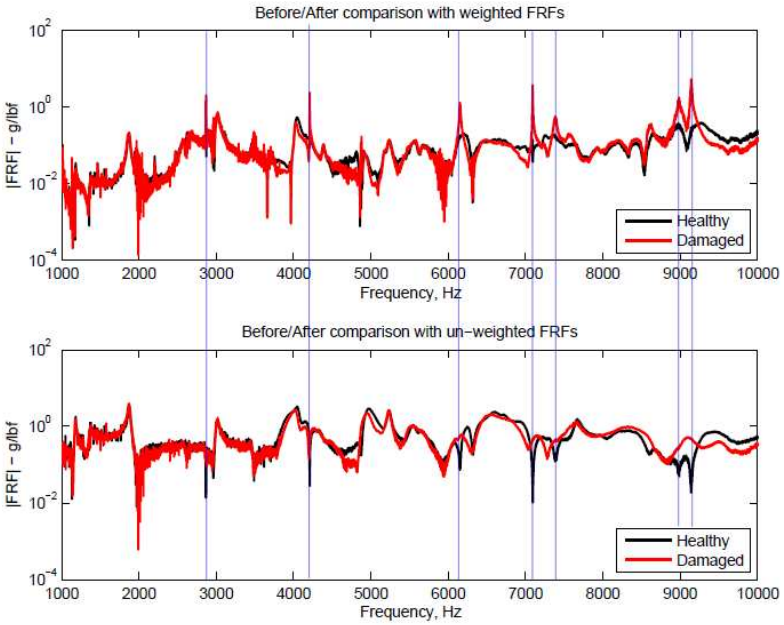

Figure 28: Data Showing Anti-resonance Problem On Composite Pressure Vessel Before And After Damage

which of the natural frequencies will change most significantly. The cantilever beam example shows that the spatial dependence of the damage changes can be used to increase the sensitivity to damage if the location of damage is known beforehand, but the composite pressure vessel example shows that this approach presents numerical challenges which make the application of this technique with a single sensor as a reference problematic.

This page intentionally left blank.

5 Non-Linear Vibration Based Damage Detection Techniques

Although linear vibration based techniques are capable of detecting changes in the structure related to damage, there are significant limitations when solely considering changes in linear dynamics. One of these limitations is that these linear vibration based techniques rely on a knowledge of the baseline vibration characteristics of the structure, so calibration of the system with a known healthy state is generally necessary. Another limitation is that while damage in composites usually starts as a very localized flaw, the linear vibration characteristics of a structure are global properties of the system, and may not substantially change if the damage is small and isolated. This global characteristic of linear vibration properties is advantageous in some ways, because changes in global stiffness or mass associated with damage or material degradation can be detected regardless of location; however, if the location of potential damage was known, nonlinear vibration based techniques could detect damage with a greater sensitivity and without a historical data set for calibration. Because the impact identification technique presented here can locate the region of interest for damage evaluation, nonlinear vibration based techniques are a promising possibility to achieve the goal of an integrated load and damage characterization system.

5.1 Nonlinear damage characteristics in composites

Prior work, including some by colleagues at Purdue, has investigated the nonlinear dynamics in damaged composite structures. For instance, Underwood showed that the response due to nonlinear dynamics caused by impact damage to composite aircraft panels could be isolated to the area of damage experimentally [56, 55, 7]. She further evaluated this idea using a model of a composite beam where an isolated core crack or disbond was modeled as a stiffness and damping nonlinearity at the location of damage, and showed that the trends observed in experiments could be explained by this damage model. A disbond in the honeycomb panel was modeled by removing the constraint between the core and the face sheet at the location of damage and allowing the face sheet to lose contact with the core when moving away from the center. This model showed a localized nonlinear response at the site of damage. By measuring the frequency response between a damage location and forcing location at two different amplitudes, and then comparing the estimated frequency responses at these two amplitudes, the nonlinearity was quantified.

Previous research has worked to quantify the nonlinear restoring forces in damaged composite panels. Brush and Adams took the approach of damaging a small test specimen, and then measuring the driving point impedance at the location of damage [10]. Restoring force diagrams were

made through this approach, which indicated that the damage produced both a reduction in the linear stiffness, and a nonlinear hardening stiffness when the face sheet was moving toward the core. Figure 29 (reproduced from [10]), shows an example restoring force diagram from this work. The higher linear stiffness of the undamaged panel is indicated by the fairly constant slope of the undamaged force vs. deflection curve, which is larger than the linear component of the damaged force vs. deflection curve. The nonlinear stiffness of the damaged test article is indicated by the increasing slope of the force vs. deflection curve for positive displacement values. Changes in damping between healthy and damaged states are also observed, but the most important trend to note for this work is the change in stiffness characteristics.

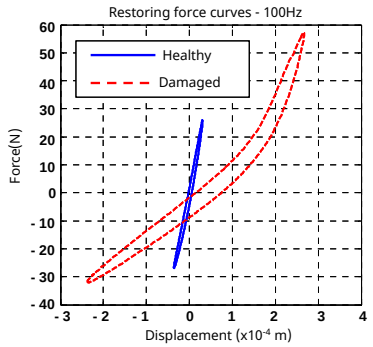

Figure 29: Comparison of restoring force curves for healthy and damaged composite sandwich panels

In related research, Dittman, a colleague from Purdue, sought to investigate the nonlinear structural dynamics of a facesheet-core disbond in a honeycomb-core sandwich panel [19, 20]. By exciting the structure and measuring the response at the site of damage using sub-harmonic, super-harmonic, and resonant frequencies, and then comparing results to those from a single degree of freedom analytical model, he was able to identify the nonlinear response form of the local dynamics at the damage site. The main strengths of this technique are in identifying the order of nonlinearities in damaged structures and identifying the presence of nonlinearities using a single frequency excitation. The most significant limitations of this technique are that the model only directly applies to systems which can be modeled as having a single degree of freedom, and that frequencies of the primary resonance must be determined before selecting the frequency of the harmonic excitation. Another slight drawback to this approach is that it focuses on nonlinearities which are expressed as a sum of polynomial functions of the displacement or velocity. Other nonlinear functions of the response could be approximated by a polynomial series and analyzed in the same way, but a large number of terms might be required to adequately capture the behavior of the system.

5.2 Nonlinear system identification approach

One approach that addresses these limitations is a nonlinear system identification technique known as Nonlinear Identification through Feedback of the Outputs (NIFO). This approach, developed by Adams and Allemang, formulates the dynamics of a nonlinear system as an underlying linear system with a nonlinear feedback loop [1]. This idea is represented in Figure 30.

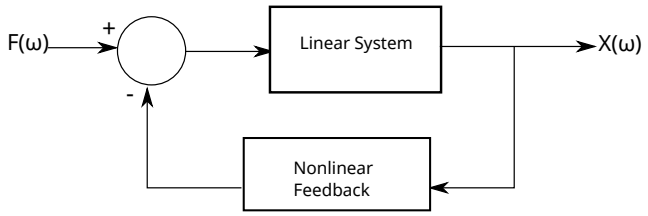

Figure 30: Nonlinear Feedback System Diagram

The advantage to this formulation is that the overall response can be considered as a multiple-input system, with the inputs to the system being a combination of true forcing functions and nonlinear functions of the outputs. Furthermore, the portion of the response due to the nonlinearity is a function of the underlying linear frequency response function. In this form, the coefficient of nonlinearity can be identified in a single step along with the frequency response of the underlying system. Assuming that we have N_i measured inputs, N_o measured outputs, N_{avg} data sets, and a single nonlinearity, then equation (28) describes the response of the structure, where $X(\omega)$ is the response, $H_L(\omega)$ is the linear frequency response matrix, μ_1 is the coefficient of nonlinearity, B_1 is a vector that describes the degree of freedom at which the nonlinear force is acting, F is a vector of forcing functions, and X_n is the nonlinear displacement.

$$[X(\omega)]_{N_o x 1} = \Big[[H_L(\omega)] \quad [H_L \omega] \mu_1(\omega) \{B_{n1}\} \Big]_{(N_o x (N_i+1))} \begin{bmatrix} [F]_{N_i x 1} \\ X_n \end{bmatrix}_{((N_i+1)x1)} \tag{28}$$

The above equation is the same form as a MIMO FRF relationship, where there are N_o output measurements, and $N_i + 1$ input measurements, with the only difference being that one of these inputs is a function of the system response, X_n. To simplify notation, the FRF matrix above can be renamed as $H_{NL} = [[H_L]\ [H_L]\mu_1\{B_{n1}\}]$, and the rightmost vector $\{F_{NL}\} = [[F],\ [X_n]]^T$. Making these substitutions, (28) becomes:

$$[X]_{N_o x 1} = \Big[H_{NL} \Big]_{(N_o x (N_i+1))} \Big[F_{NL} \Big]_{((N_i+1)x1)} \tag{29}$$

Treating F_{NL} as a standard forcing vector, and H_{NL} as a standard FRF matrix, H_{NL} can be estimated using standard MIMO FRF estimation techniques. In this case, the H_2 FRF estimator that considers several data sets is used. Once the matrix $[H_{NL}]$ is estimated, the underlying linear frequency response function matrix and the coefficient of nonlinearity can be found in a single step. The first N_i columns of H_{NL} are H_L, and the last column is equal to the product $H_L \mu_1 B_{n1}$.

The strength of this technique is that it decouples the system's linear and nonlinear response characteristics provided that the location and form of the nonlinearity is well understood. In essence, this approach uses spatial data to improve the system identification results. Among other applications, Haroon and Adams have shown that this technique can be used to identify the nonlinear characteristics of vehicle suspension systems [28].

The nonlinear characteristics of composite damage, as summarized above, make this technique well suited to quantifying damage effects. The spatial nature of this technique makes sense in the context of this work because this nonlinear damage identification would be carried out after identifying the location of potentially damaging impacts, using the entropy-based impact identification algorithm developed here. By using this impact location data, the difficulty in quantifying the coefficient of nonlinearity is substantially reduced. Furthermore, this approach helps to isolate the nonlinear effects associated with one particular damage event.

5.3 Experimental setup

In order to test this idea of nonlinear system identification for composite damage evaluation, a simple test was conducted with simulated damage on a 6"x36" fiberglass honeycomb sandwich panel. A piezoelectric actuator was attached to a skewed mounting block through an impedance head to excite the structure. The response was measured using triaxial accelerometers mounted to the top and bottom face sheets at the edge of the panel, as shown in Figure 31. Two types of forcing functions were tested: sine sweeps and band-limited white noise. For either excitation signal, the panel was tested at several excitation amplitude levels. After the healthy response was measured, core crack damage was simulated by cutting the core with a knife in between two of the accelerometers. The size of the core cut was increased incrementally, and the panel was tested at each step. The simulated damage at its maximum size is shown in Figure 32.

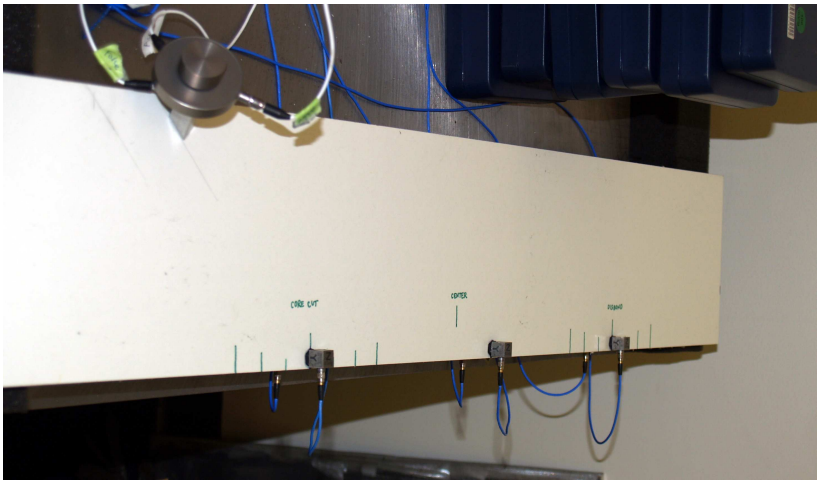

Figure 31: Test Setup Showing Actuator At The Upper Left Of The Image, And The Six Accelerometers Which Were Used Along The Bottom Edge

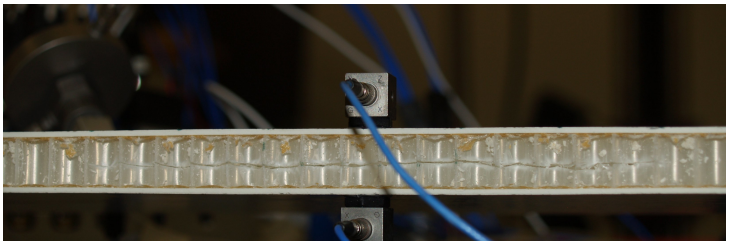

Figure 32: Simulated Core-crack Damage For The Largest Crack Size

5.4 Results

Initial findings from this test show promise for this technique. For the purposes of this report we will focus on one of the damage levels, with results from two of the forcing function amplitude levels which we used.

A comparison of the frequency response of the damaged structure when forced at two amplitude levels one initial check of the data that is useful for guiding the data analysis. If the panel responds in a nonlinear way as observed by Underwood, the frequency response estimates of the damaged structure will be somewhat different between the high and low forcing functions, and the frequencies at which these differences occur will give some indications of the frequency ranges where nonlinear response characteristics are present. Figure 33 shows this comparison of frequency response functions when the structure is forced at two amplitude levels. On a perfectly linear structure, these functions would be identical. However, there are differences in this case, which indicates that the structure is responding in a nonlinear fashion. The changes between high

and low amplitude FRFs are apparent at the anti-resonances at approximately 320, 400, and 700 Hz, near the peak in the 600-700Hz range, and, most significantly, between 750-900Hz.

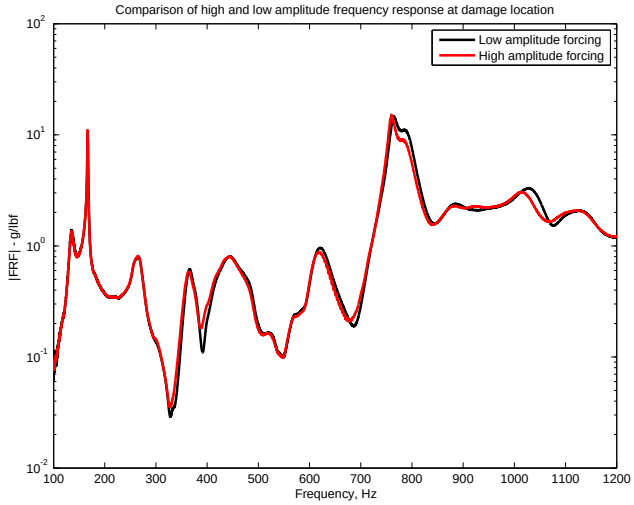

Figure 33: Comparison Of Frequency Response Function At Damage Location Using High And Low Amplitude Forcing Functions

The forcing and response data for the damaged panel using the same amplitude levels shown in Figure 33 were used in the NIFO algorithm to attempt to separate the linear and nonlinear response at the site of damage. Although several assumed nonlinear functions were tested, we will focus on one of these functions for this discussion. Recall from the discussion of the NIFO technique, an assumed nonlinear displacement, x_n, must be used in the estimation process. Building off of Underwood and Brush's work in characterizing similar damage mechanisms, we assumed that the panel responded with a hardening spring when the core was under compression at the site of damage, and a linear, low stiffness spring when the core was in tension. The assumed nonlinear displacement which represented this behavior is given in equation (30), where x_{top} and x_{bottom} are the response above and below the simulated damage, and in the direction normal to the surface.

$$x_n = 1/2 * (x_{top} - x_{bottom})^2 (1 - \text{sgn}(x_{top} - x_{bottom})) \tag{30}$$

The NIFO technique was applied to estimate the underlying linear frequency response function and the coefficient of nonlinearity. Since only one level of damage was analyzed, there is little context for the coefficient of nonlinearity, so the estimated linear frequency response function is considered first. In Figure 34, the estimated linear frequency response function is compared to the measured frequency response function (i.e. the estimated FRF assuming a completely linear structure) at the location of damage. If the structure behaved linearly, or if the assumed nonlinear

function did not match the actual nonlinearity in the structure, these two curves would be approximately the same. In the frequency range below 300Hz, the two functions are nearly identical, which is consistent with the observations from the high and low amplitude frequency response function comparison. This showed that the structure behaved in a largely linear manner at that frequency range. At the frequencies where the system behaved nonlinearly, these two functions are very different. However, the estimated linear FRF also assumes a very unusual shape in some frequency ranges where it differs from the linear FRF, particularly in the 600-700Hz range. The differences in the 700-800Hz range seem more plausible. The source of this apparent error is unclear at this point, but it may be attributable to either numerical error or an assumed nonlinear function which does not match the actual behavior of the system.

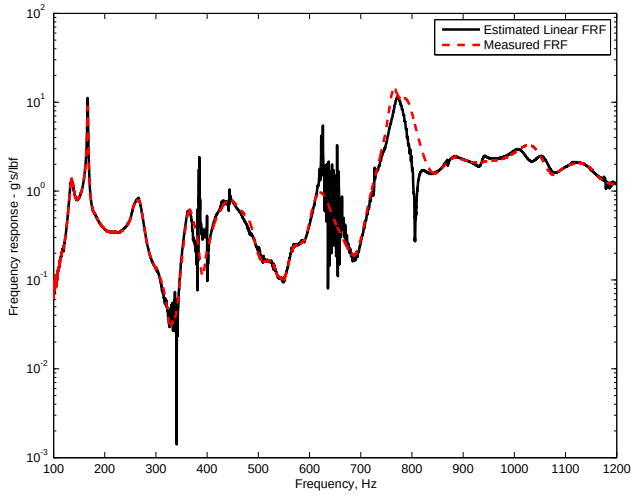

Figure 34: Comparison Of Measured Frequency Response Function And Estimated Linear Frequency Response Function From NIFO

Approaches for improving NIFO estimates have been developed, and employing these approaches has the potential to improve results. Particularly of interest is the work of SM Spottswood, who showed that the nonlinear characteristics of a beam-like structure could be better identified with reduced order modeling [52]. His work used a modal decomposition of the structure, and he was able to better estimate nonlinear parameters using this approach than when implementing the NIFO approach directly. This approach holds promise for detecting localized changes, because the assumed deflection shapes used in reduced order modeling could potentially separate the local effects of the damage from the global vibration properties of the structure.

5.5 Conclusions

Nonlinear damage identification techniques, as presented here, have the potential to overcome many of the difficulties associated with linear vibration based damage identification techniques. These techniques have the potential to identify damage despite changes in environmental conditions or boundary conditions because the baseline frequency response function measurement does not need to be compared directly. In particular, the nonlinear identification technique shown here, based on a nonlinear frequency domain model, has the potential to quantify specific nonlinearities by using spatial information. The use of spatial information is important for this application because the impact identification technique, which was presented in earlier chapters, can identify the location of potential damage. This damage identification technique could be used alongside the impact load identification technique to evaluate the presence and/or extent of damage associated with a particular impact.

An experiment studying the effects of a crack in the core of a sandwich panel showed significant nonlinear response at the location of damage, and the frequency ranges at which the highest nonlinear contribution was found matched expectations from prior techniques. While future work will be needed to apply these techniques in full, these results suggest that there is potential for identifying nonlinear damage characterstics by utilizing the spatial information gained from impact identification.

6 Conclusions and Recommendations for Future Work

6.1 Impact Load Identification

The primary goal of this work was to address the challenges of structural health monitoring for impact damage on large composite structures. To this end, we have presented a method for identifying impact forces and locations using as few as one sensor, even on a very large structure. By studying how the impact force estimates are effected by the location of the sensor, we have shown that this technique is insensitive to sensor location, and the projected uncertainty in impact estimates using a particular sensor configuration can be evaluated before monitoring. To further enhance this impact identification technique, we have developed an uncertainty quantification technique which evaluates the quality of impact force estimates in real time based on the entropy of the recreated force estimates. With implementation issues such as sensor placement studied, and methods for presenting the impact estimates along with credible confidence intervals established, this impact identification technique has been significantly matured through this work. Future work on this impact identification technique will address the final details needed to deploy this technology on operational aircraft and other structures. The most significant of these details that must be addressed for deployment are listed below:

1. Reduction and/or cancellation of steady state operational noise.
2. Compensation for boundary and loading conditions of the structure in operation.
3. Minimization of training data required.

Reduction of operational noise is an important consideration, particularly for lower amplitude impacts, because excessive noise on response measurements can decrease the accuracy of force estimates. Excessive noise can also degrade the force localization technique because very noisy force estimates from the correct location are difficult to distinguish from force estimates from an incorrect location. While this is a significant implementation challenge, however, it is somewhat ameliorated by the uncertainty quantification technique which was developed in this work. Unreliable force magnitude and location estimates which are a result of excessive noise will have significantly higher recreated force entropy, which we have shown is an indicator of uncertainty of the impact.

Another implementation challenge is compensating for boundary and loading conditions which do not match those of the structure during model training. These boundary condition changes can

arise for a variety of reasons, but most commonly, the reason for the change in boundary conditions is that the structure with operational boundary and loading conditions cannot be measured. For instance, if this method were applied to operational rotor blades, (e.g. wind turbine, helicopter), the structural dynamics during operation would be significantly different from those in the static configuration.

An experiment studying the effects of a crack in the core of a sandwich panel showed significant nonlinear response at the location of damage, and the frequency ranges at which the highest nonlinear contribution was found matched expectations from prior techniques. While future work will be needed to apply these techniques in full, these results suggest that there is potential for identifying nonlinear damage characterstics by utilizing the spatial information gained from impact identification. Because modal impact testing of the blades at operational speeds would not be practical or even possible in most instances, the structure would need to be measured at rest, and the frequency response functions which were measured on the static structure would need to be compensated for the altered boundary conditions. Approaches for this compensation are being developed in separate work by colleagues at Purdue and Vanderbilt University, but further work is necessary to create a deployable solution for challenging applications such as rotor blades.

6.2 Impact Damage Identification

Utilizing an assumed location of damage was shown to enhance the ability of linear vibration based techniques to detect structural changes related to damage. Tests on the lap splice specimen showed how structural dynamic changes at a specific location affected some modes more so than others, and that the modes at which the dynamics changed significantly were evident based on the associated mode shapes. A simple analytical model of a beam with a localized stiffness reduction showed how this idea could be used to enhance the sensitivity of remote measurements to damage if the location of damage were known. Therefore, by combining the impact localization techniques presented earlier, the sensitivity of remote measurements to damage could be potentially increased. By weighting response measurements with a transmissability filter based on measurements of the healthy structure, the modes which change substantially can be emphasized, and therefore the effects of damage can be enhanced.

The application of this technique to a more complex geometry introduced some challenges to the use of this location-based filter for weighting. Numerical issues at frequencies where anti-resonances exist have the potential to indicate high levels of damage at a particular location even if the relevant structural changes were elsewhere. Future work could examine how this problem

could be addressed through multiple response measurements and solving an overdetermined inverse problem for a transmissability filter which is less affected by numerical issues. Nevertheless, this technique shows how even simple linear vibration-based techniques can be enhanced to detect localized damage if the location of damage is estimated through impact identification.

By further investigating nonlinear damage identification techniques, many of the difficulties associated with linear vibration based damage identification techniques can be overcome. The need for a baseline healthy measurement is reduced or eliminated for most of these nonlinear damage evaluation techniques, and therefore structural and boundary condition changes have less of an effect. Furthermore, some of these nonlinear damage detection methods can provide an order of magnitude increase in damage indicators, because the nonlinear response metrics can increase as a function of the square, cube, or higher power of the nonlinear damage coefficient [19].

6.3 Integrated Impact Load and Damage Identification

The idea of combining the tasks of load and damage evaluation has great potential for multiple aviation and civil health monitoring applications. Many other SHM techniques could be enhanced by this knowledge of the impact location. For instance, changes in local stiffness or damping could be evaluated directly through embedded sensitivity functions if the location of potential damage were known. The idea of embedded sensitivity functions is that the sensitivity of a frequency response function to changes in structural properties can be expressed in terms of frequency response function estimates directly, without an analytical model. One of the largest practical limitations of this technique is that the location of damage must be known; it estimates the change in structural properties between specific degrees of freedom. By combining this impact identification technique with embedded sensitivity functions, future work could identify the local change in structural stiffness associated with a particular impact.

The strength of this integrated load and damage identification technique is that methods which were previously not practical for global damage assessment on a large structure can be utilized on a much larger scale. Some of these techniques are used for "hot spot" damage detection, where a problematic area of the structure is identified and monitored closely, but by combining information about impact locations with damage identification techniques in real time, many of these localized approaches could be implemented over a broader area of the structure. By integrating impact load and damage identification for structural health monitoring, it will be possible to obtain a real time indication of the damage severity, and significantly aid the maintenance and lifecycle management of large composite structures.

This page intentionally left blank.

References

[1] DE Adams and RJ Allemang. A frequency domain method for estimating the parameters of a non-linear structural dynamic model through feedback. *Mechanical Systems and Signal Processing*, 14(4):637–656, 2000.

[2] Douglas Adams, Jonathan White, Mark Rumsey, and Charles Farrar. Structural health monitoring of wind turbines: method and application to a HAWT. *Wind Energy*, 14(4):603–623, 2011.

[3] A.G. Miller, D.T. Lovell, and J.C. Seferis. The Evolution of an Aerospace Material: Influence of Design, Manufacturing and In-Service Performance. *Composite Structures*, 27(1-2):193–206, 1994.

[4] S Atobe, H Fukunaga, and N Hu. Impact Force Identification of CFRP Structures Using Experimental Transfer Matrices. *Computers Materials and Continua*, 26(1):67, 2011.

[5] G. Bartelds. Aircraft Structural Health Monitoring, Prospects for Smart Solutions From a European Viewpoint. *Structural Health Monitoring, Current Status and Perspectives*, pages 293–300, 1997.

[6] Ivan Bartoli, Salvatore Salamone, Francesco Lanza di Scalea, Jennifer Rhymer, and Hyonny Kim. Impact force identification in aerospace panels by an inverse ultrasonic guided wave problem. pages 79841F–79841F–11, 2011.

[7] R Bond, S Underwood, D Adams, and J Cummins. Structural health monitoring-based methodologies for managing uncertainty in aircraft structural life assessment. In *Proceedings of 9th International Workshop on Structural Health Monitoring*, August 2013. Manuscript submitted and under review.

[8] Z. Boukria, P. Perrotin, A. Bennani, F. Dupray, and A. Limam. Structural monitoring: identification and location of an impact on a structurally dissipating rock-shed structure using the inverse method. *European Journal of Environmental and Civil Engineering*, 16(1):20–42, 2012.

[9] J.C. Briggs. *Force Identification using Extracted Modal Parameters, with Applications to Glide Height Testing of Computer Hard Disks*. PhD thesis, Massachusetts Institute of Technology, 1991.

[10] E Brush. Development of a dynamic model for subsurface damage in sandwich composites. Master's thesis, Purdue University, 2009.

[11] B.T. Wang and C.H. Chiù. Determination of Unknown Impact Force Acting on a Simply Supported Beam. *Mechanical Systems and Signal Processing*, 17(3):683–704, 2003.

[12] C. Budde. Impact Force Identification for Composite Helicopter Blades Using Minimal Sensing. Master's thesis, Purdue University, August 2010.

[13] C. Budde, N.C. Yoder, D.E. Adams, P. Meckl, and D. Koester. Impact Detection for Fiberglass Composite Rotor Blade. 2009.

[14] C. Chang and C.T. Sun. Determining transverse impact force on a composite laminate by signal deconvolution. *Experimental Mechanics*, 29(4):414–419, 1989.

[15] Keeyoung Choi and Fu-Kuo Chang. Identification of impact force and location using distributed sensors. *AIAA journal*, 34(1):136–142, 1996.

[16] Francesco Ciampa, Michele Meo, and Ettore Barbieri. Impact localization in composite structures of arbitrary cross section. *Structural Health Monitoring*, 11(6):643–655, 2012.

[17] C.C. Ciang, J.R. Lee, and H.J. Bang. Structural health monitoring for a wind turbine system: a review of damage detection methods. *Measurement Science and Technology*, 19(12):122001, 2008.

[18] D. Cripps. The future of blade repair. *Reinforced Plastics*, 55(1):28–32, 2011.

[19] E Dittman. *Identification and quantification of nonlinear behavior in a disbonded aluminum honeycomb panel using single degree-of-freedom models*. PhD thesis, Purdue University, 2013.

[20] E Dittman and D Adams. Detection and quantification of a disbonded aluminum honeycomb panel using nonlinear superharmonic frequencies. In *Proceedings of 9th International Workshop on Structural Health Monitoring*, August 2013.

[21] J.F. Doyle. A wavelet deconvolution method for impact force identification. *Experimental Mechanics*, 37(4):403–408, 1997.

[22] Hisao Fukunaga and Ning Hu. Damage Monitoring of CFRP Structures Based on Impact Force Identification. 2006.

[23] A. Ghoshal, M.J. Sundaresan, M.J. Schulz, and P. Frank Pai. Structural health monitoring techniques for wind turbine blades. *Journal of Wind Engineering and Industrial Aerodynamics*, 85(3):309–324, 2000.

[24] Daniel Guyomar, Mickaël Lallart, Thomas Monnier, Xingjun Wang, and Lionel Petit. Passive Impact Location Estimation Using Piezoelectric Sensors. *Structural Health Monitoring*, 8(5):357–367, 2009.

[25] H. Inoue, K. Kishimoto, T. Shibuya, and T. Koizumi. Estimation of Impact Load by Inverse Analysis: Optimal Transfer Function for Inverse Analysis. *JSME International Journal. Ser. 1, Solid Mechanics, Strength of Materials*, 35(4):420–427, 1992.

[26] J.J. Harrigan H. Inoue and S.R. Reid. Review of Inverse Analysis for Indirect Measurement of Impact Force. *Applied Mechanics Reviews*, 54:503, 2001.

[27] Berthold Hahn, Michael Durstewitz, and Kurt Rohrig. Reliability of wind turbines. In *Wind Energy*, pages 329–332. Springer, 2007.

[28] Muhammad Haroon and Douglas E. Adams. A modified {H2} algorithm for improved frequency response function and nonlinear parameter estimation . *Journal of Sound and Vibration*, 320(4–5):822–837, 2009.

[29] B. Hayman, J. Wedel-Heinen, and P. Brondsted. Materials challenges in present and future wind energy. *Warrendale: Materials Research Society*, 2008.

[30] N Hu, H Fukunaga, S Matsumoto, B Yan, and XH Peng. An efficient approach for identifying impact force using embedded piezoelectric sensors. *International journal of impact engineering*, 34(7):1258–1271, 2007.

[31] Ning Hu and Hisao Fukunaga. A new approach for health monitoring of composite structures through identification of impact force. *Journal of Advanced Science*, 17(1+2):82–89, 2005.

[32] Shun-Fa Hwang and Guu-Huann Liu. Buckling behavior of composite laminates with multiple delaminations under uniaxial compression. *Composite structures*, 53(2):235–243, 2001.

[33] Byeong-Wook Jang, Yeon-Gwan Lee, Jin-Hyuk Kim, Yoon-Young Kim, and Chun-Gon Kim. Real-time impact identification algorithm for composite structures using fiber Bragg grating sensors. *Structural Control and Health Monitoring*, 19(7):580–591, 2012.

[34] K. Choi and F.K. Chang. Identification of Impact Force and Location Using Distributed Sensors. *AIAA journal*, 34(1):136–142, 1996.

[35] C. Kong, S. Choi, and H. Park. Investigation on Design for a 500 W Wind Turbine Composite Blade Considering Impact Damage. *Advanced Composite Materials*, 20(2):105–123, 2011.

[36] Seungmin Kwon, Jintai Chung, and Hong Hee Yoo. Structural dynamic modeling and stability of a rotating blade under gravitational force. *Journal of Sound and Vibration*, (0):–, 2013.

[37] Dong Liang, Shen-fang Yuan, and Meng-long Liu. Distributed coordination algorithm for impact location of preciseness and real-time on composite structures. *Measurement*, 46(1):527–536, 2013.

[38] E. Lourens, E. Reynders, G. De Roeck, G. Degrande, and G. Lombaert. An augmented Kalman filter for force identification in structural dynamics. *Mechanical Systems and Signal Processing*, 27(0):446–460, 2012.

[39] V Mallardo, M H Aliabadi, and Z Sharif Khodaei. Optimal sensor positioning for impact localization in smart composite panels. *Journal of Intelligent Material Systems and Structures*, 24(5):559–573, 2013.

[40] Johannes F. C. Markmiller and Fu-Kuo Chang. Sensor Network Optimization for a Passive Sensing Impact Detection Technique. *Structural Health Monitoring*, 9(1):25–39, 2010.

[41] N. Stites, C. Escobar, J. White, D.E. Adams, and M. Triplett. Quasi-active, Minimal-Sensing Load and Damage Identification and Quantification Techniques for Filament-Wound Rocket Motor Casings. volume 6532, page 65321E. SPIE, 2007.

[42] Byeongjin Park, Hoon Sohn, Steven E Olson, Martin P DeSimio, Kevin S Brown, and Mark M Derriso. Impact localization in complex structures using laser-based time reversal. *Structural Health Monitoring*, 11(5):577–588, 2012.

[43] J H Park, Y S Moon, and S K Lee. Source localization of multiple impacts in a plate. *Proceedings of the Institution of Mechanical Engineers, Part C: Journal of Mechanical Engineering Science*, 226(2):423–438, 2012.

[44] Jonghyun Park and Fu-Kuo Chang. System identification method for monitoring impact events. In *Proc. SPIE*, volume 5758, pages 189–200, 2005.

[45] Jonghyun Park, Sungwon Ha, and Fu-Kuo Chang. Monitoring impact events using a system-identification method. *AIAA journal*, 47(9):2011–2021, 2009.

[46] Dennis Roach, Stephen Neidigk, and FAA Airworthiness Assurance Center. Does the maturity of Structural Health Monitoring technology match user readiness? In *Proceedings of the 8th International Workshop on Structural Health Monitoring*, volume 11, 2011.

[47] M Ruiz, L E Mujica, X Berjaga, and J Rodellar. Partial least square/projection to latent structures (PLS) regression to estimate impact localization in structures. *Smart Materials and Structures*, 22(2):025028, 2013.

[48] Robert Seydel and Fu-Kuo Chang. Impact identification of stiffened composite panels: I. System development. *Smart Materials and Structures*, 10(2):354, 2001.

[49] Robert Seydel and Fu-Kuo Chang. Impact identification of stiffened composite panels: II. Implementation studies. *Smart materials and structures*, 10(2):370, 2001.

[50] C.E. Shannon. A Mathematical Theory of Communication. *The Bell System Technical Journal*, 27:623–656, 1948.

[51] Z Sharif-Khodaei, M Ghajari, and M H Aliabadi. Determination of impact location on composite stiffened panels. *Smart Materials and Structures*, 21(10):105026, 2012.

[52] S.M. Spottswood and R.J. Allemang. Identification of nonlinear parameters for reduced order models . *Journal of Sound and Vibration*, 295(1–2):226–245, 2006.

[53] N. Stites. Minimal-Sensing Passive and Semi-Active Load and Damage Identification Techniques for Structural Components. Master's thesis, Purdue University, August 2007.

[54] Nick Stites and Douglas E. Adams. Semi-active Damage Identification for a Composite Structural Missile Component using Minimal Passive Sensing with Data-driven Models. *Journal of Intelligent Material Systems and Structures*, 20(3):337–353, 2009.

[55] S Underwood. *Subsurface damage detection in sandwich composites using three-dimensional laser vibrometry measurements with nonlinear vibration response characteristics*. PhD thesis, Purdue University, August 2012.

[56] S Underwood, D Adams, and J Meyer. Damage Localization in Composite Structures Using Nonlinear Vibration Response Properties. Manuscript in preparation.

[57] Det Norske Veritas. Offshore Standard DNV-OS-J102 Design and Manufacture of Wind Turbine Blades, Offshore and Onshore Wind Turbines, 2006.

[58] D.N. Veritas. Design and Manufacture of wind turbine blades. *Offshore and Onshore Wind Turbines*, 1, 2006.

[59] Jonathan R White, Douglas E Adams, and Mark A Rumsey. Operational load estimation of a smart wind turbine rotor blade. In *The 16th International Symposium on: Smart Structures and Materials & Nondestructive Evaluation and Health Monitoring*, pages 72952D–72952D. International Society for Optics and Photonics, 2009.

[60] W.J. Cantwell and J. Morton. The Impact Resistance of Composite Materials–a Review. *Composites*, 22(5):347–362, 1991.

[61] W.J. Cantwell, P.T Curtis, and J. Morton. Low Velocity Impact Damage Tolerance in C.F.R.P. Laminates Containing Woven and Non-Woven Layers. *Composites*, 14(3):301–305, 1983.

[62] Qingsong Xu. Impact Detection and Location for a Plate Structure using Least Squares Support Vector Machines. *Structural Health Monitoring*, 2013.

[63] Gang Yan and Li Zhou. Impact load identification of composite structure using genetic algorithms. *Journal of Sound and Vibration*, 319(3–5):869–884, 2009.

[64] HongJun Yang, Young Jun Lee, and Sang Kwon Lee. Impact source localization in plate utilizing multiple signal classification. *Proceedings of the Institution of Mechanical Engineers, Part C: Journal of Mechanical Engineering Science*, 227(4):703–713, 2013.

[65] Nathanael C Yoder, Douglas E Adams, and Matt Triplett. Multidimensional sensing for impact load and damage evaluation in a carbon filament wound canister. *Materials evaluation*, 66(7):756–763, 2008.

This page intentionally left blank.

George Akhras
Centre for Smart Materials & Structures
Kingston, ON, Canada

David Anderson
Boeing
Seattle, WA

Fernanda Aredes
Embraer
Sao Jose Dos Campos, Brazil

Mohammad Azarbayejani
University of New Mexico
Albuquerque, NM

Anil Bajaj
Purdue University
West Lafayette, IN

John Bakuckas
FAA
Atlantic City, NJ

Krishnan Balasubramaniam
Indian Institute of Technology Madras
Chennai, India 600036

David Baldwin
University of Oklahoma
Norman, OK

Robert J. Barthorpe
University of Sheffield
Sheffield, UK

Preston Bates
Sikorsky Aircraft
Stratford CT

Ivan Bartoli
UC-San Diego
La Jolla. CA

Gregory Bartram
Vanderbilt University
Nashville, TN

Ray Beale
Sikorsky Aircraft
Stratford CT

Nick Bellinger
National Research Council Canada
Ottawa, Canada

Blake Bertrand
Boeing
Seattle, WA

Jaen Marc Bertrand
Bombardier Aerospace
Montreal, Canada

Wolfgang Bisle
Airbus
Bremen, Germany

Clemens Bockenheimer
Airbus
Bremen, Germany

John Bohler
Delta Air Lines
Atlanta, GA

Christian Boller
Fraunhofer Institute
Saarbruckern, Germany

Richard Bossi
Boeing
Seattle, WA

Michael Bouchard
University of Dayton Research Institute
Dayton, OH

John Brigham
University of Pittsburgh
Pittsburgh, PA

Andrew Brookhart
Sikorsky Aircraft
Stratford CT

Matthias Buderath
EADS Deutschland
Munich, Germany

Sander Carneiro
Agencia Nacional De Aviacao Civil
Sao Jose dos Campos SP, Brazil

Fabio Cascati
University of Pavia
Pavia, Italy

Sara Casciati
University of Catania
Siracusa, Italy

Fu-Kuo Chang
Stanford University
Stanford, CA

Todd Chapman
Boeing
Seattle, WA

Carlos Chaves
Embraer
São José dos Campos, Brazil

Eric Chesmar
United Airlines
San Franscisco, CA

Wingkong Chiu
Monash University,
Clayton, Australia

Antonio Concilio
CIRA
Capua Caserta, Italy

Dale Cope
Southwest Research Institute
San Antonio, TX

Melba Crawford
Purdue University
West Lafayette, IN

Chris Davis
Boeing
Seattle, WA

Mark Davis
Sikorsky Aircraft
Stratford CT

Dacama Del Olmo
EADS
Madrid, Spain

Paula Dempsey
NASA Glenn Research Center
Cleveland, OH

Michael Derby
U.S. Department of Energy
Washington, D.C.

Mark Derriso
US Air Force
Wright Patterson AFB, OH

Jacques Desjardins
Bombardier
St-Bruno, Quebec Canada

Fernando Dotta
Embraer
Sao Jose Dos Campos, Brazil

Christopher Earls
Cornell University
Ithaca, NY

Lucia Faravelli
University of Pavia
Pavia, Italy

Spilios Fassois
University of Patras
Patras, Greece

Jozue Vieira Filho
Sao Paulo State University
Ilha Solteira/SP, Brazil

Rafael Foltran
Agencia Nacional De Aviacao Civil
Sao Jose dos Campos, Brazil

Peter Foote
Cranfield University
Bedfordshire, United Kingdom

Andrew Freese
Air New Zealand
Aukland, New Zealand

Mark Freisthler
FAA
Renton, WA

Hisao Fukunaga
Tohoku University
Sendai, Japan

Steve Galea
Defence Science Technology Organization
Fishermans Bend, Australia

David Galella
FAA Tech Center
Atlantic City Intl, NJ

Gary Georgeson
Boeing
Seattle, WA

Hamid Ghasemi
Federal Highway Administration
McLean, VA

Keith Gilmore
Continential Airlines
Houston, TX

Victor Giurgiutiu
Univ. of South Carolina
Columbia, SC

Camila Gonsalez
Embraer
São José dos Campos, Brazil

Ignacio Gonzalez
Universidad Politecnica de Madrid
Madrid, Spain

Grant Gordon
Honeywell
Phoenix, AZ

Alfredo Guemes
Polytechnic University of Madrid
Madrid, Spain

Seyit Ali Gungor
Fokker Aircraft Services B.V.
Hoogerheide, Netherlands

Alex Guo
Stanford University
Stanford, CA

Luis Gustavo Dos Santos
Embraer
Sao Jose Dos Campos, Brazil

Marvin Hamstad
University of Denver
Denver, CO

Artur Hanc
EC Electronics
Krakow, Poland

Colin Hanna
Bombardier Aerospace
Belfast, United Kingdom

Ulrike Hanskoetter
Airbus
Bremen, Germany

Joel Harley
Carnegie Mellon Univ.
Pittsburgh, PA

Sophie Hasbroucq
Eurocopter
Cedex, France

Eric Haugse
Boeing
Seattle, WA

Alastair Healey
European Aviation Safety Agency
Koln, Germany

Daniel Hebért
Transport Canada
Ottawa, Ontario Canada

Peter Heer
Lufthansa Technik AG
Frankfurt, Germany

Jaap Heida
National Aerospace Laboratory NLR
Emmeloord, The Netherlands

Rudolf Henrich
Airbus
Bremen, Germany

Gwanghee Heo
Konyang University
Nonsan, Korea

Keiji Hirabayashi
All Nippon Airways
Ota-ku Tokyo, Japan

Wolfgang Hoffmann
EASA
Cologne, Germany

Edward Hohman
Bell Helicopter Textron
Hurst, TX 76053

Quincy Howard
Boeing
Seattle, WA

Haiying Huang
University of Texas at Arlington
Arlington, TX 76019

Lem Hunter
Vibrant Corporation
Albuquerque, NM

Dryver Huston
University of Vermont
Burlington, VT

Heli Hytti
Tampere University of Technology
Tampere, Finland

Jeong-Beom Ihn
Boeing
Seattle, WA

Larry Ilcewicz
FAA
Seattle, WA

Erik A. Johnson
University of Southern California
Los Angeles, CA

Rusty Jones
FAA
Washington, DC

Seth Kessler
Metis Design Corporation
Cambridge, MA

Junichi Kimoto
Kawasaki Heavy Industries, LTD.
Kakamigahara City, Gihu-Pref., Japan

Jeffrey Kollgaard,
Boeing
Seattle, WA

Michael Kolling
Airbus
Hamburg, Germany

Kenneth Knopp
FAA
Atlantic City, NJ

Jerzy Komorowski
National Research Council Canada
Ottawa, Quebec Canada

Marek Krawczuk
Polish Academy of Sciences
Gdansk, Poland

Iddo Kressel
Israel Aerospace Industries
Israel

Sridhar Krishnaswamy
Northwestern Univ., Dept. of Mech. Engr.
Evanston. IL

Walter Kruse
NM Institute of Mining &Technology
Socorro, NM

P. Kudela
Polish Academy of Sciences
Fiszera 14 St, Gdansk, Poland

Francesco Lanza di Scalea
University of California San Diego
La Jolla, CA

Silvia Lazcano
Airbus Orperations SL
Madrid, Spain

Dy Le
Army Research Laboratory
Aberdeen Proving Ground, MD

Syun Lee
China Airlines
Taoyuan, Taiwan

Arne Lewis
Boeing
Seattle, WA

Glenn Light
Southwest Research Institute
San Antonio, TX

John Linn
Boeing
Seattle, WA

Cliff Lissenden
Penn State
University Park, PA

George Liu
US Army
Redstone Arsenal, AL

Yongming Liu
Clarkson University
Potsdam, NY

Israel Lopez
UC Davis
Davis, CA

Mark Lopez
Air Transport Association
Washington, DC

Marc Lord
Transport Canada (TCCA)
Ottana, Ontario, Canada

Joe Lougheed
Lockheed Martin
Marietta, GA

Ye Lu
University of Sydney
Sydney, Australia

Sankaran Mahadevan
Vanderbilt University
Nashville, TN

Pawel Malinowski
Polish Academy of Sciences
Gdansk, Poland

Pekka Manninen
Finnair
Vantaa, Finland FIN

Marek Krawczuk
Polish Academy of Sciences
Gdansk, Poland

Marcias Martinez
Technische Universiteit Delft
Delft, Netherlands

Patrice Masson
Universite de Sherbrooke
Sherbrooke, QC, Canada

Junya Matsuda
Japan Airlines International Co., Ltd.
Everett, WA

Jim McFeat
BAE Systems
Preston Lancashire, United Kingdom

Robert Menezes
Messier-Dowty
Gloucester, UK

Viviana Meruane
Universidad de Chile
Leuven, Belgium

Brian Mesing
Bell Helicopter Textron Inc
Hurst, TX

Thomas Messervey
D'Appolonia S.p.A.
Genova, Italy

Jennifer E. Michaels
Georgia Tech
Atlanta, GA

Andy Miller
Air New Zealand
Christchurch, New Zealand

Shu Minakuchi
Univ. of Tokyo
Chiba, Japan

Akira Mita
Keio University
Yokohama, Japan

Eric Mitchell
American Airlines
Tulsa, OK

Takeshi Miyashita
Nagoaka University of Technology
Nagaoka, Japan

Subhasish Mohanty
Arizona State University
Tempe, AZ,

Tommy Mullis
USAF, WRALC/ENGN
Robins AFB, GA

Hideaki Murayama
The University of Tokyo
Tokyo, Japan

Jeong Na
University of Dayton Research Institute
Dayton, OH

Ramaswamy Nagarajan
University of Massachusetts Lowell
Lowell, MA

Tamotsu Nagasaka
All Nippon Airways
Tokyo, Japan

Christopher Niezrecki
UMass Lowell
Lowell, MA

Toshimichi Ogisu
Fuji Heavy Industries, Ltd.
Utsunomiya, Japan

Yoji Okabe
The University of Tokyo
Tokyo, Japan

Steven Olson
University of Dayton Research Institute
Dayton, OH

Wieslaw Ostachowicz
Polish Academy of Sciences
Gdansk, Poland

Costas Papadimitriou
University of Thessaly
Volos, Greece

Georgios Papageorgiou
Olympic Airways
Spata, Greece

Jeff Peiter
Delta Air Lines
Atlanta, GA

Ricardo Perera
Technical University of Madrid
Madrid, Spain

Luiz Perin
Embraer
São José dos Campos, Brazil

Kara Peters
North Carolina State University
Raleigh, NC

Jerome Pinsonnault
Bombardier
Montreal, Canada

David Piotrowski
Delta Airlines
Atlanta, GA

William Prosser
NASA
Hampton, VA

Carlo Rainieri
StreGa Lab - University of Molise
Termoli, Italy

Nick Rajic
DSTO
Melbourne, Australia

Stephan Rapp
Technische Universität München
Garching, Germany

Jeff Rhoads
Purdue University
West Lafayette, IN

Ricardo Rulli
Embraer
Sao Jose Dos Campos, Brazil

Paul Rutherford
Boeing Research and Technology
Seattle, WA

Patrick Safarian
FAA
Seattle, WA

Fernando Santos
Airbus/Testia
Toulouse, France

Michael Scheerer
Austrian Institute of Technology
Seibersdorf, Austria

Sahra Sedigh
Missouri Univ. of Science and Technology
Rolla,MO

Paulo Anchieta da Silva
Embraer
Sao Jose dos Campos, Brazil

Clyde Simmerman,
US Navy
Patuxent River, MD

Holger Speckmann
Airbus
Bremen, Germany

Ippei Susuki
Japan Aerospace Exploration Agency
Mitaka, Tokyo, Japan

Paul Swindell
FAA
Atlantic City, NJ

Uhl Tadeusz
University of Science and Technology
Krakow, Poland

Mahmoud Taha
University of New Mexico
Albuquerque, NM

Takeda, Nobuo
The University of Tokyo
Chiba, Japan

Michael Todd
University of California San Diego
La Jolla, CA 92093

Simon Waite
European Aviation Safety Agency
Koln, Germany

Dong Wang
The University of Sydney
Sydney, NSW, Australia

Ed Weinstein
FAA
Atlantic City, NJ

Lorenz Wenk
Airbus
Hamburg, Germany

David Westlund
FAA
Atlantic City, NJ

Bill Winfree
NASA
Hampton, VA

Ian Won
FAA
Seattle, WA

Jun Yamanaka
Japan Airlines
Ota-ku Tokyo, Japan

Philip Yannaccone
American Airlines
Tulsa, OK

Nathanael C. Yoder
Purdue University
Lafayette, IL

Rick Young
NASA
Hampton, VA

Theriault Yves
Bombardier Aerospace
Dorval, Canada

Andrei Zagrai
New Mexico Tech
Socorro, NM

Daniele Zonta
University of Trento
Trento, Italy

Glen Zs Guo
Shanghai University
Shanghai, China

Sandia National Labs:

1 Paul Hommert
6000 Jill Hruby
6121 David Minster
6121 Joshua Paquette
6121 Jonathan White
6122 Todd Griffith
6122 Daniel Laird
6600 Billy Marshall
6610 Jeff Danneels
6620 Roberto Mata
6620 Willy Morse
6620 Dennis Roach
6621 Michel Bode
6621 Andrea Dorado
6621 Randy Duvall
6621 Steve Heffelfinger
6621 Stephen Neidigk
6621 Tom Rice
6622 Robert Baca
6623 Mark Soo Hoo
6625 Barry Boughton
6630 Brad Parks
7911 Donna Chavez
7911 Yolanda Moreno
8040 Marcey Hoover
9532 Recorded Information Management

Sandia National Laboratories